A NEW GENERATION OF PARTICLE-BASED RADIO FREQUENCY (RF) SWITCHES FOR PORTABLE AND HIGH-FREQUENCY APPLICATIONS

A Thesis
Submitted to the Graduate Faculty
of the
North Dakota State University
of Agriculture and Applied Science

By

Nasim Soufizadeh Balaneji

In Partial Fulfillment of the Requirements
for the Degree of
MASTER OF SCIENCE

Major Department:
Electrical and Computer Engineering

April 2019

Fargo, North Dakota

NORTH DAKOTA STATE UNIVERSITY

Graduate School

Title

A NEW GENERATION OF PARTICLE-BASED RADIO FREQUENCY (RF)
SWITCHES FOR PORTABLE AND HIGH-FREQUENCY APPLICATIONS

By

Nasim Soufizadeh Balaneji

The supervisory committee certifies that this thesis complies with North Dakota State University's regulations and meets the accepted standards for the degree of

MASTER OF SCIENCE

SUPERVISORY COMMITTEE:

Dr. Benjamin D. Braaten
Chair

Dr. Alan R. Kallmeyer

Dr. David A. Rogers

Approved:

10 April 2019
Date

Dr. Benjamin D. Braaten
Department Chair

ABSTRACT

Reconfigurable and tunable designs which provide multi-functionality are highly desirable in wireless communication systems. Amongst different methodologies to design RF switching, a directly connected biasing circuitry is not required for Static Field Micro-Particle Components (SFM-PCs); therefore, not only power consumption is lowered but also these particle-based switches can be used in complex geometries. However, the traditional structure has low-frequency bandwidth for both ON and OFF states and fails to operate correctly when undergoing rotation, these result in difficulties in using them in portable higher band applications. To address these issues, here two new techniques to increase the frequency bandwidth of ON and OFF states were proposed. Furthermore, a novel 360-degree rotatable structure was developed. The efficacy of these structures were evaluated by embedding them into discontinuous microstrip transmission lines. Both HFSS simulations and measurements show the accuracy of the analysis and the efficacy of the proposed designs.

ACKNOWLEDGEMENTS

I would like to pay my regards to the people below who made my research successful and assisted me at every point to cherish my goal:

- My family members who not only assisted me financially but also extended their support morally and emotionally.

- Dr. Alan R. Kallmeyer, chair of the Department of Mechanical Engineering, for his vital support and sympathetic attitude during my studies at NDSU; his involvement in my research made it possible to achieve the goal.

- Dr. David A. Rogers, professor in the Department of Electrical and Computer Engineering, and Dr. Sylvio May, chair of the Department of Physics, Dr. Benjamin Braaten, chair of the Department of Electrical and Computer Engineering, for their guidance and contributions to this research work.

DEDICATION

To my Parents

To my Siblings

Thank you for your unconditional love and encouragement.

TABLE OF CONTENTS

LIST OF TABLES

Table Page

LIST OF FIGURES

LIST OF APPENDIX FIGURES

1. INTRODUCTION

Multi functionality of a single device can be achieved by turning ON/OFF the embedded RF switches. These RF switches, which can be components such as PIN diodes [1] [2] [3], RF MEMS, and Field Effect Transistors (FETs), enable the designs of reconfigurable antennas/arrays [4] and filters. While they provide benefits to the RF systems, each of these methodologies pose limitations in terms of frequency response, power consumption, and isolation loss. PIN diodes are one of the common building blocks in RF systems; however, they exhibit relatively high insertion loss, low linearity, and high power consumption [5] [6] [7]. RF MEMS switches are another switching methodology which have low power consumptions but they suffer from expensive manufacturing techniques [8] [9] [10] [11] [12]. Finally, FET based switches not only require extra power but also are susceptible to overload voltages [13]. While using RF switches allows for more than one operational mode for each design, their embodiment into the host structure might either lead to performance degradation or increase the overall power consumption. Thereby, based on the requirements of an application such as -3 dB frequency, isolation loss, and power consumption, the type of the switch should be chosen. Hence, devoting efforts to design new switching techniques is a must.

The need for a biasing network or lumped elements including RF chokes and bypass capacitors in order to control the ON or OFF states of these components, not only increases the overall power consumption of RF systems, but also requires careful design to prevent performance degradation. In order to address these challenges, recently a particle-based switch has been developed [14] and has been used in different applications including transmission lines [14], reconfigurable antennas [15], and filters [16]. This particle-based switch does not require DC biasing circuitry for its operation [14] [17] [18] and addresses the main challenges of other methodologies such as the need for an RF choke in PIN diodes [19], high manufacturing cost and electrical noise in MEMS [19], and extra power consumption in FETs; however, not only the frequency band for the ON and OFF states of the traditional SFM-PC based switches are limited to only few hundred megahertz but also they fail to operate correctly when they undergo rotations, making it difficult to embed these switches into the products where rotation is inevitable. Therefore, in order to address the needs of the growing communication market, SFM-PC switches featuring high-frequency bandwidth for both ON and OFF states as well as reliable operation for 360-degree rotation should be developed.

2. ANALYSIS OF TRADITIONAL SINGLE SWITCH SYMMETRIC COPPER (SSWSC) STATIC FIELD MICRO-PARTICLE COMPONENT (SFM-PC)

Fig. 2.1 illustrates the traditional Single Switch Symmetric Copper (SSwSC) Switch embedded on a host substrate with the relative permittivity of ϵ_{sb} and thickness of h_{sb}; note that the host substrate can be a discontinuous microstrip printed transmission line (TL) [14], a reconfigurable filter, or a reconfigurable antenna. The switch, made of the dielectric material with the relative permittivity ϵ_{sw}, width w_{sw}, length l_{sw}, and height h_{sw}, consists of a cylindrical cavity drilled out of it and is filled with micron-sized silver-coated magnetite core particles up to the height αh_{sw} where $0 < \alpha < 1$. The switch is placed on part PR_1 of the host and its top side is connected to the part PR_2 of the host using symmetric copper foil with the widths of $w_1 = w_2 = w_3$ as labeled in Fig. 2.1(a). The two parts of the host structure, PR_1 and PR_2, are isolated by a gap with a length l_g.

In order to understand the functionality of the traditional particle based switch, the ON and OFF states will be analyzed separately.

2.1. ON State

As can be seen from Fig. 2.1(b), upon applying a static magnetic field, the particles stack on top of each other to create columns in the direction of the field lines. These columns connect

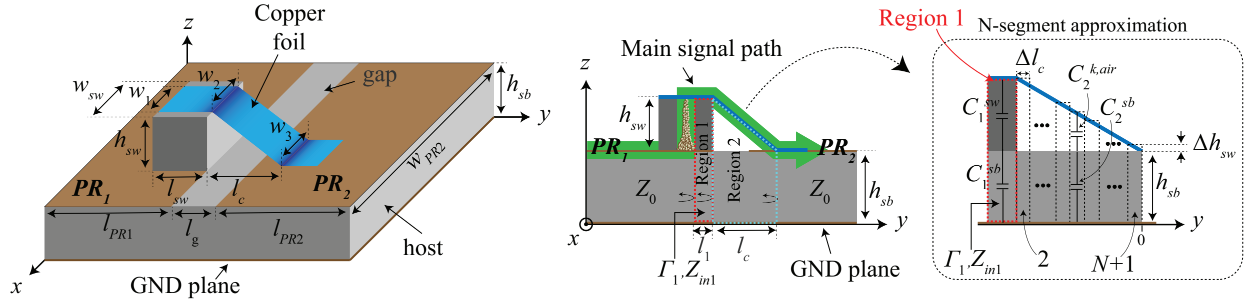

(a) (b) (c)

Figure 2.1. (a) Placement of traditional Single Switch Symmetric Copper SFM-PC with symmetric copper foil ($w_1 = w_2 = w_3$) on a host substrate, (b) main signal path for the ON state, and (c) N-segment approximation for the second region, labeled from 2 to $N + 1$.

the two parts PR_1 and PR_2 of the host together to increase the propagation area of the antenna, to transfer the signal from the input port to the output port of the transmission line [14] or the filter [16]. Considering quasi-TEM mode, when the switch turns on, the signal travels through the substrate material between the GND plane and the main signal path consisting of PR_1, stacked micron-sized particles, copper foil, and PR_2 as shown by a green arrow in Fig. 2.1(b). Note that it is assumed that the coupling signal through the shaded area of the switch is negligible compared to the main signal path.

Due to the embodiment of the switch on the substrate, two regions called 1 and 2 with characteristic impedances of $Z_{0,1}$ and $Z_{0,2}$ were created; the dotted lines in Fig. 2.1(b) show the boundary between different regions. When the signal travels through the substrate and reaches the boundary between the ith and jth regions, one of the following cases will occur

- $Z_{0,i} = Z_{0,j} \rightarrow$ all of the signal transfers to the jth region, in other words, $\Gamma_i = 0$.
- $Z_{0,i} \neq Z_{0,j} \rightarrow$ fraction of the signal reflects from the boundary, making $|\Gamma_i| > 0$.

Therefore, to obtain $\Gamma_1^{SSwSC} = 0$, the characteristic impedances of different regions should have the same values as that of the substrate. Assuming a lossless medium along the signal path, the characteristic impedance of the first and second region can be expressed as

$$Z_{0,i} = \sqrt{\frac{L_i}{C_i}} \qquad i = 1 \text{ and } 2, \tag{2.1}$$

where L_i represents the series inductance per unit length of the signal path in the ith region and C_i is the shunt capacitance per unit length in ith region between the signal path and GND plane. The capacitance and inductance per unit length for each region were extracted: 1) using the characteristic impedance of the microstrip transmission line for the width to the height ratio greater than or equal to unity [20] and 2) assuming $\epsilon = c\sqrt{L_i C_i}$, where ϵ is the dielectric constant and $c = 3\text{e}8$ m/sec.

For simplicity in expressing the equations, the function $f(x, y) = \frac{x}{y} + 1.393 + 0.667 \ln(\frac{x}{y} + 1.444)$ was defined and used in order to formulate the parameters in the ith region which are L_i, C_i, and $Z_{0,i}$. Utilizing function f, for the host microstrip transmission line, the following equations can be calculated for inductance per unit length, capacitance per unit length, and characteristic impedance, respectively.

$$L_0 = \frac{120\pi}{f(w_t, h_{sb})c}, \tag{2.2}$$

$$C_0 = \frac{\epsilon_{sb} f(w_t, h_{sb})}{120\pi c}, \tag{2.3}$$

and

$$Z_0 = \sqrt{\frac{L_0}{C_0}} = \frac{120\pi}{\sqrt{\epsilon_{sb}} f(w_t, h_{sb})}, \tag{2.4}$$

where w_t is the trace width and h_{sb} is the height of the transmission line (TL), respectively.

2.1.1. Region 1

As illustrated in Fig. 2.1(c), this region consist of two capacitances in series; C_1^{sw} and C_1^{sb} which can be defined as

$$C_1^{sw} = \frac{\epsilon_{sw} f(w_{sw}, h_{sw})}{120\pi c}, \tag{2.5}$$

and

$$C_1^{sb} = \frac{\epsilon_{sb} f(w_{sw}, h_{sb})}{120\pi c}. \tag{2.6}$$

The total capacitance per unit length in this region, which is C_1^{sw} and C_1^{sb} in series can be obtained from

$$C_1 = \frac{C_1^{sw} C_1^{sb}}{C_1^{sw} + C_1^{sb}} = \frac{\epsilon_{sw} f(w_{sw}, h_{sw}) f(w_{sw}, h_{sb})}{f(w_t, h_{sb})\Big(\epsilon_{sw} f(w_{sw}, h_{sw}) + \epsilon_{sb} f(w_{sw}, h_{sb})\Big)} C_0, \tag{2.7}$$

where C_0 is from (2.3).

The inductance per unit length in the first region can be calculated from the equation given below in which L_0 is from (2.2).

$$L_1 = \frac{120\pi}{f(w_{sw}, h_{sb} + h_{sw})c} = \frac{f(w_t, h_{sb})}{f(w_{sw}, h_{sb} + h_{sw})} L_0. \tag{2.8}$$

Using (2.7) and (2.8), the characteristic impedance in region 1 can be formulated as

$$Z_{0,1} = \sqrt{\frac{L_1}{C_1}} = Z_0 \times D_1, \tag{2.9}$$

where D_1 is the ratio of the characteristic impedance of region 1 to that of the host and is given by

$$D_1 = \sqrt{\frac{f^2(w_t, h_{sb})\Big(\epsilon_{sw} f(w_{sw}, h_{sw}) + \epsilon_{sb} f(w_{sw}, h_{sb})\Big)}{\epsilon_{sw} f(w_{sw}, h_{sw}) f(w_{sw}, h_{sb}) f(w_{sw}, h_{sb} + h_{sw})}} \tag{2.10}$$

2.1.2. Region 2

Unlike the first region which has the constant height over the length $l_1 = \frac{l_{sw}-2r}{2}$, in the second region, the height of the copper foil ranges from h_{sw} to zero along l_c. In order to analyze this region and consequently provide an intuitive understanding about the functionality of the switch, the copper foil in this region was approximated with N segments with length $\Delta l_c = \frac{l_c}{N}$ and height $\Delta h_{sw} = \frac{h_{sw}}{N}$ as shown in Fig. 2.1(c). Note that 2-segment, 3-segment, and 4-segment approximations could be found in the appendix.

The series combination of $C_2^{k,air}$ and C_2^{sb} creates the total capacitance per unit length in the kth segment which can be calculated from

$$C_2^k = \frac{C_2^{k,air} C_2^{sb}}{C_2^{k,air} + C_2^{sb}} = \frac{f(w_{sw}, h_2^k) f(w_{sw}, h_{sb})}{f(w_t, h_{sb})\Big(f(w_{sw}, h_2^k) + \epsilon_{sb} f(w_{sw}, h_{sb})\Big)} C_0 \tag{2.11}$$

The inductance per unit length and the characteristic impedance of the kth segment in the second region are given by (2.12) and (2.13), respectively.

$$L_2^k = \frac{f(w_t, h_{sb})}{f(w_{sw}, h_2^k + h_{sb})} L_0 \tag{2.12}$$

and

$$Z_{0,2}|_k = \sqrt{\frac{L_2^k}{C_2^k}} = Z_0 D_2^k, \tag{2.13}$$

where

$$D_2^k = \sqrt{\frac{f^2(w_t, h_{sb})\Big(f(w_{sw}, h_2^k) + \epsilon_{sb} f(w_{sw}, h_{sb})\Big)}{f(w_{sw}, h_2^k + h_{sb}) f(w_{sw}, h_2^k) f(w_{sw}, h_{sb})}} \tag{2.14}$$

Using the characteristic impedance values of the first region plus the N segments of the second region, $Z_{0,1}$ and $Z_{0,2}|_k$ (where $k = 2, \cdots, N{+}1$) , the voltage reflection coefficient (Fig. 2.1(b)) can be written as

$$\Gamma_1^{SSwSC} = \frac{Z_{in1} - Z_0}{Z_{in1} + Z_0} = \frac{\Gamma_1^{SSwSC}|_{Num.}}{\Gamma_1^{SSwSC}|_{Den.}}, \tag{2.15}$$

where its numerator and denominator are given by (2.16) and (2.17):

$$\begin{aligned}
\Gamma_1^{SSwSC}|_{Num.} = {} & \sum_{i=1}^{N+1} j\Big(\prod_{b_p \in B_i^1} D_{b_p}\Big)\Big(\prod_{a_q \in A_i^1} \tan(\beta_{a_q} l_{a_q})\Big)\Big((D_{a_q})^2 - 1\Big) \\
& + \sum_{m=2}^{N} \Big(\sum_{i=1}^{\binom{N+1}{m}} j^m \big(\prod_{b_p \in B_i^m} D_{b_p}\big)\big(\prod_{a_q \in A_i^m} \tan(\beta_{a_q} l_{a_q})\big)\big(\prod_{\substack{q\ odd \\ a_q \in A_i^m}} (D_{a_q})^2 - \prod_{\substack{q\ even \\ a_q \in A_i^m}} (D_{a_q})^2\big)\Big) \\
& + j^{N+1}\big(\prod_{a_q \in A_i^{N+1}} \tan(\beta_{a_q} l_{a_q})\big)\big(\prod_{\substack{q\ odd \\ a_q \in A_i^{N+1}}} (D_{a_q})^2 - \prod_{\substack{q\ even \\ a_q \in A_i^{N+1}}} (D_{a_q})^2\big)
\end{aligned} \tag{2.16}$$

$$\begin{aligned}
\Gamma_1^{SSwSC}|_{Den.} = {} & 2 \times \big(\prod_{i \in U} D_i\big) + \sum_{i=1}^{N+1} j\Big(\prod_{b_p \in B_i^1} D_{b_p}\Big)\Big(\prod_{a_q \in A_i^1} \tan(\beta_{a_q} l_{a_q})\Big)\Big((D_{a_q})^2 + 1\Big) \\
& + \sum_{m=2}^{N} \Big(\sum_{i=1}^{\binom{N+1}{m}} j^m \big(\prod_{b_p \in B_i^m} D_{b_p}\big)\big(\prod_{a_q \in A_i^m} \tan(\beta_{a_q} l_{a_q})\big)\big(\prod_{\substack{q\ odd \\ a_q \in A_i^m}} (D_{a_q})^2 + \prod_{\substack{q\ even \\ a_q \in A_i^m}} (D_{a_q})^2\big)\Big) \\
& + j^{N+1}\big(\prod_{a_q \in A_i^{N+1}} \tan(\beta_{a_q} l_{a_q})\big)\big(\prod_{\substack{q\ odd \\ a_q \in A_i^{N+1}}} (D_{a_q})^2 + \prod_{\substack{q\ even \\ a_q \in A_i^{N+1}}} (D_{a_q})^2\big),
\end{aligned} \tag{2.17}$$

where

$\Big\{A_i^m\Big\}$: is the collection of $i(=\binom{N+1}{m})$ subsets of $U = \{1, 2, \cdots, N+1\}$ with size m

$A_i^m = \Big\{a_1, \cdots, a_q, \cdots, a_m\Big\}$ in which $a_q < a_{q+1}$

$\Big\{B_i^m\Big\}$: is the collection of i subsets of $U = \{1, 2, \cdots, N+1\}$ with size $N+1-m$

$B_i^m = \Big\{b_1, \cdots, b_p, \cdots, b_{N+1-m}\Big\}$ such that $B_i^m \cup A_i^m = U$ and $B_i^m \cap A_i^m = \varnothing$

From (2.16), it can be concluded that in order to reduce the voltage reflection coefficient, the coefficient D in each region should go to 1.0.

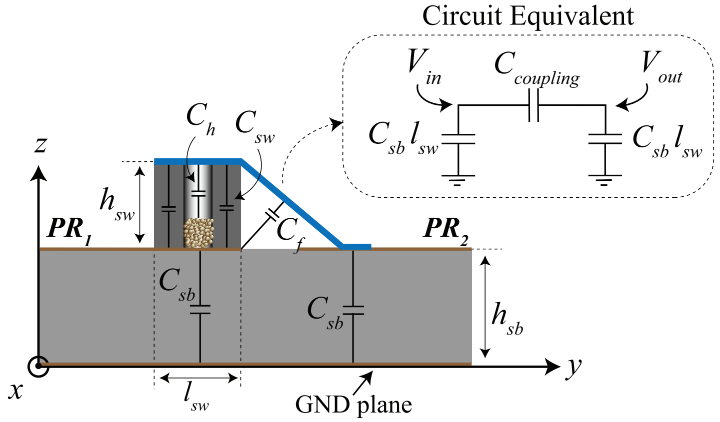

Figure 2.2. Coupling voltage to the output though the capacitance for the OFF state.

2.2. OFF State

Fig. 2.2 shows the side view of the traditional SFM-PC on the host structure for the OFF state [18]. When the magnetic field intensity ($\overline{H}$) becomes zero, the particles settle at the bottom of the cavity due to gravitational force. In other words, the two parts of the host, PR_1 and PR_2, become disconnected as the SFM-PC switch is off. However, due to the coupling capacitance, a high-frequency input signal might appear in the output port of an RF system, resulting in low isolation.

Based on the equivalent circuit shown in Fig. 2.2, the relationship between the output and input signals can be written as

$$V_{out}^{SSwSC} = \frac{C_{coupling}}{C_{coupling} + C_{sb}l_{sw}} \times V_{in} \tag{2.18}$$

and from [14]

$$C_{coupling} = C_{sw} + C_h + C_f \simeq C_{sw} + C_h, \tag{2.19}$$

where C_f is the fringing capacitance between the edge of the PR_1 and the copper foil; this capacitance can be neglected due to its small value [14]. By substituting the capacitance of hole and the switch, the coupling capacitance can be calculated as

$$C_{coupling} = \frac{\epsilon_0}{h_{sw}}\big(\epsilon_{sw}w_{sw}l_{sw} + \pi r^2(\frac{1}{1-\alpha} - \epsilon_{sw})\big), \tag{2.20}$$

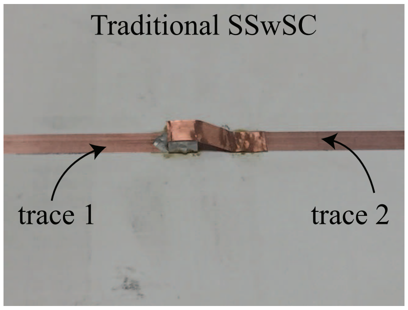

Figure 2.3. Fabricated prototype of the traditional Single Switch Symmetric Copper (SSwSC) embedded on a TL.

where

$$C_h = \epsilon_0 \frac{\pi r^2}{(1-\alpha)h_{sw}} \tag{2.21}$$

and

$$C_{sw} = \frac{\epsilon_0 \epsilon_{sw}}{h_{sw}}(w_{sw}l_{sw} - \pi r^2). \tag{2.22}$$

While the second term in the parenthesis of (2.20) can be negative or positive depending on the dielectric constant of the switch (ϵ_{sw}) and the amount of the micron-sized particle (α), in either case, its value is negligible with respect to the first term. From (2.20), it can be concluded that, while increasing the height of the switch (h_{sw}) reduces the capacitively coupled voltage, decreasing the dielectric constant of the switch (ϵ_{sw}), the width of the switch (w_{sw}), and the length of the switch (l_{sw}) improves the performance in the OFF state [21].

2.3. Simulation and measurement results

The effects of the physical characteristic of the particle-based switch were evaluated by embedding SFM-PC on a host printed microstrip transmission line (TL). The TL was designed from Rogers TMM4 material with the relative permitivity $\epsilon_r = 4.7$, thickness $h_{sb} = 1.524$ mm, top and bottom copper cladding of $t_{cu} = 0.5\ oz$, and area of 80 mm × 80 mm. The width of the transmission line traces were calculated as 2.79 mm using Advanced Design System (ADS) software; with gap length $l_g = 2$ mm in order to minimize the fringing capacitance, caused by the noncontinuous TL on the performance of the design.

The traditional Single Switch Symmetric Copper (SSwSC) with the height $h_{sw} = 1.524$ mm and dimension $w_{sw} \times l_{sw} = 3.0$ mm × 3.0 mm was designed from different dielectric materials

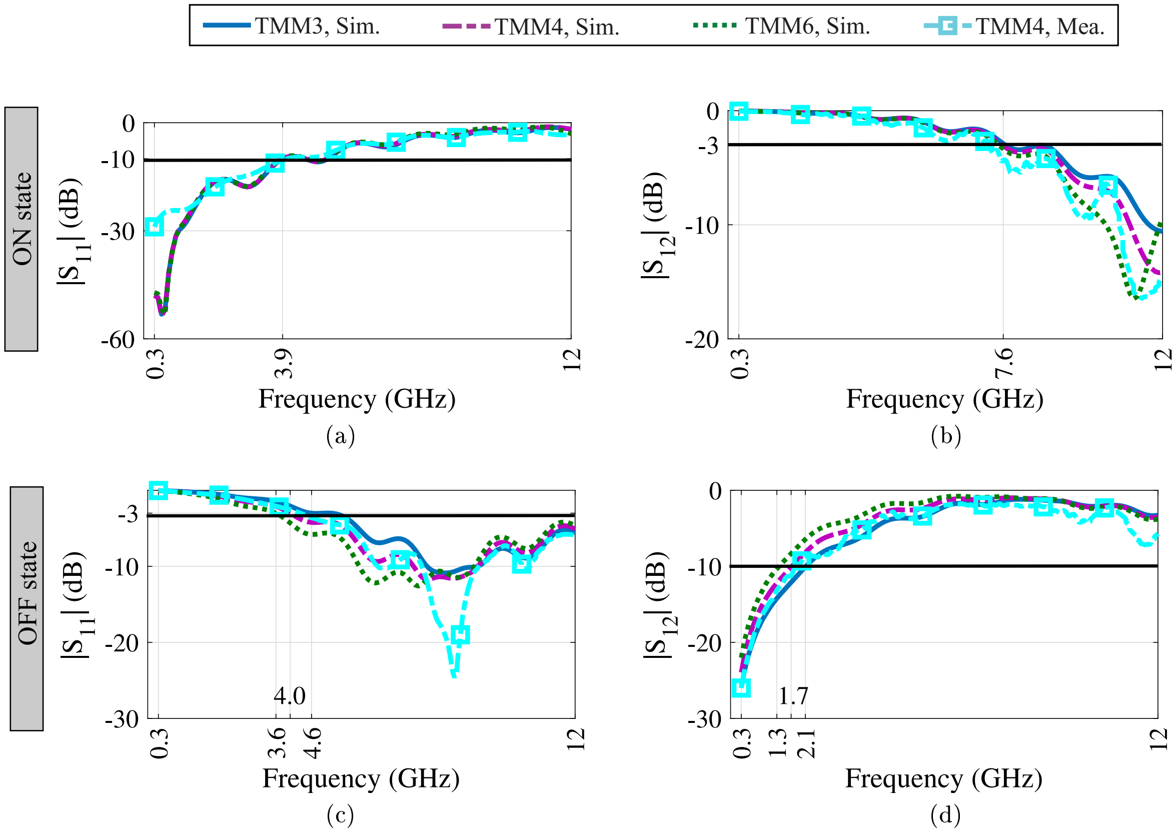

Figure 2.4. HFSS simulation and measurement results of the traditional SSwSC for various dielectric materiels including Rogers TMM3, Rogers TMM4, and Rogers TMM6 (a) $|S_{11}|$ for ON state, (b) $|S_{12}|$ for ON state, (c) $|S_{11}|$ for OFF state, and (d) $|S_{12}|$ for OFF state.

including Rogers TMM3 ($\epsilon_{sw} = 3.45$ and $\tan\delta = 0.002$), TMM4 ($\epsilon_{sw} = 4.7$ and $\tan\delta = 0.002$) and TMM6 ($\epsilon_{sw} = 6.3$ and $\tan\delta = 0.0023$). Fig. 2.4 shows the $|S_{11}|$ and $|S_{12}|$ of the embedded switch on the transmission line for both ON and OFF states. As can be seen from these, while the -10 dB frequency of $|S_{11}|$ and -3 dB of the $|S_{12}|$ of the ON state for all the dielectric materials are the same, TMM3 has a higher frequency bandwidth for the OFF state compared to other dielectric materials. This is because Rogers TMM3 material has lower relative permittivity than others, resulting in lower coupling capacitance and higher frequency bandwidth.

The effect of switch height (h_{sw}) on the performance was examined by considering three different heights: 0.762 mm, 1.524 mm, and 3.18 mm. The switch for all the heights was made of Rogers TMM4 dielectric material with the dimension $w_{sw} \times l_{sw} = 3.0$ mm $\times$ 3.0 mm. Fig. 2.5 shows the performance of the switch for different heights. While h_{sw}= 0.762 mm shows higher frequency bandwidth for the ON state compared to the others, its -3 dB frequency of $|S_{11}|$ and -10

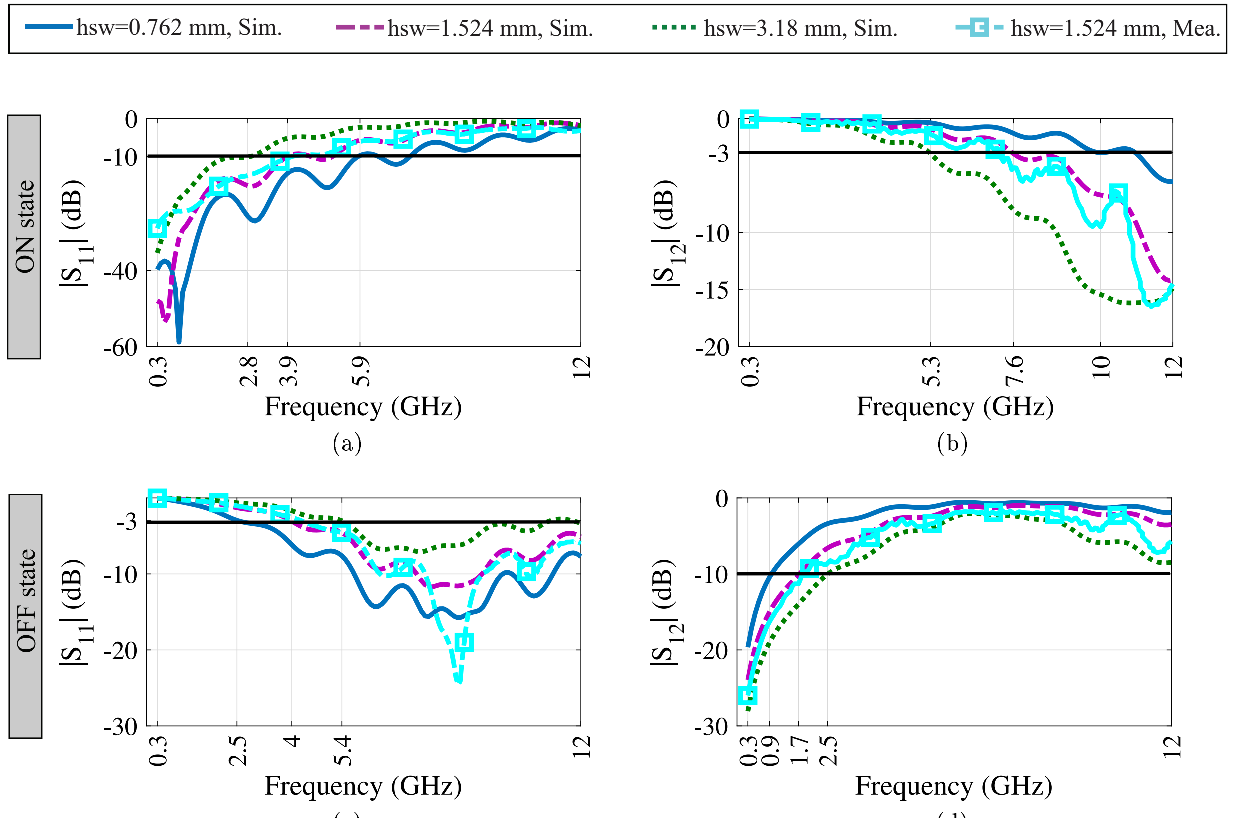

(a)

(b)

(c)

(d)

Figure 2.5. HFSS simulation and measurement results of the traditional SSwSC for $h_{sw} = 0.762$ mm, 1.524 mm, and 3.18 mm (a) $|S_{11}|$ for ON state, (b) $|S_{12}|$ for ON state, (c) $|S_{11}|$ for OFF state, and (d) $|S_{12}|$ for OFF state.

dB frequency of $|S_{12}|$ for the OFF state are the lowest. We can conclude that there is a tradeoff for the height of the switch; while reducing the height improves the frequency bandwidth of the ON state, increasing h_{sw} causes higher frequency bandwidth for the OFF state.

The traditional SFM-PC switch made of Rogers TMM4 with the height h_{sw}= 1.524 mm was used to evaluate the effects of the switch length on the performance of both ON and OFF states. Fig. 2.6 depicts the S-parameters of the ON and OFF states for three different lengths: $l_{sw} = 2$ mm, 3 mm, and 4 mm. As can be seen from the figures, reducing the length of the switch improves the frequency bandwidths of both ON and OFF states.

Finally, the effects of the width of the switch on the performance of the ON and OFF states were evaluated. Three traditional SFM-PC switches with length 3 mm, height 1.524 mm, and widths 2.0 mm, 3.0 mm, and 4.0 mm were made of Rogers TMM4 material. Illustrated in Fig. 2.7, while changing the width of the switch does not have any effect on its ON state performance, the

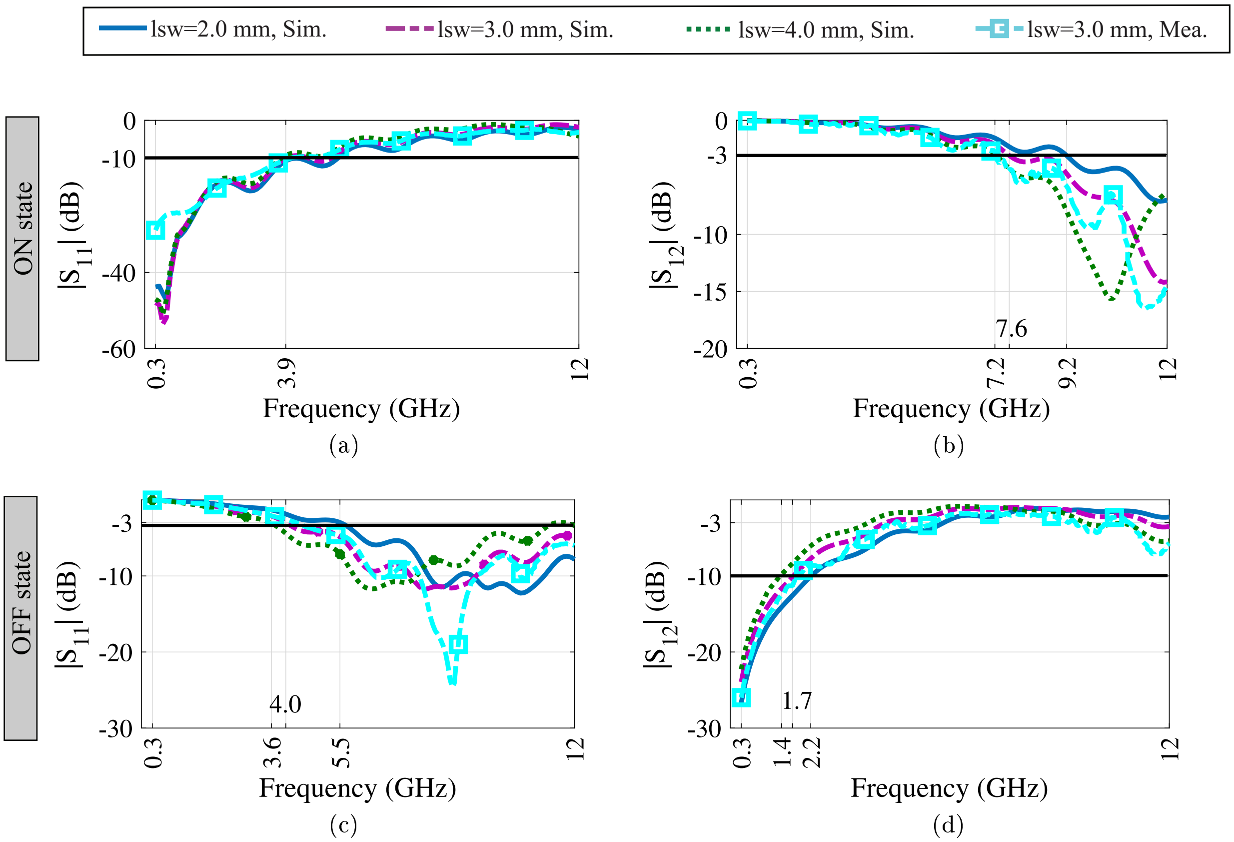

(a) (b) (c) (d)

Figure 2.6. HFSS simulation and measurement results of the traditional SSwSC for $l_{sw} = 2.0$ mm, 3.0 mm, and 4.0 mm (a) $|S_{11}|$ for ON state, (b) $|S_{12}|$ for ON state, (c) $|S_{11}|$ for OFF state, and (d) $|S_{12}|$ for OFF state.

frequency bandwidth of the switch for the OFF state is reduced for large widths due to the larger coupling capacitance.

2.4. Conclusion

In this chapter, it was shown that reducing the height and length of the switch increases the frequency bandwidth of the ON state, whereas decreasing the dielectric constant, width, and length, as well as increasing the height of the switch, provide better isolation during the OFF state. Therefore, the requirement of the high-speed devices can be satisfied by properly adjusting the physical characteristic of the switch.

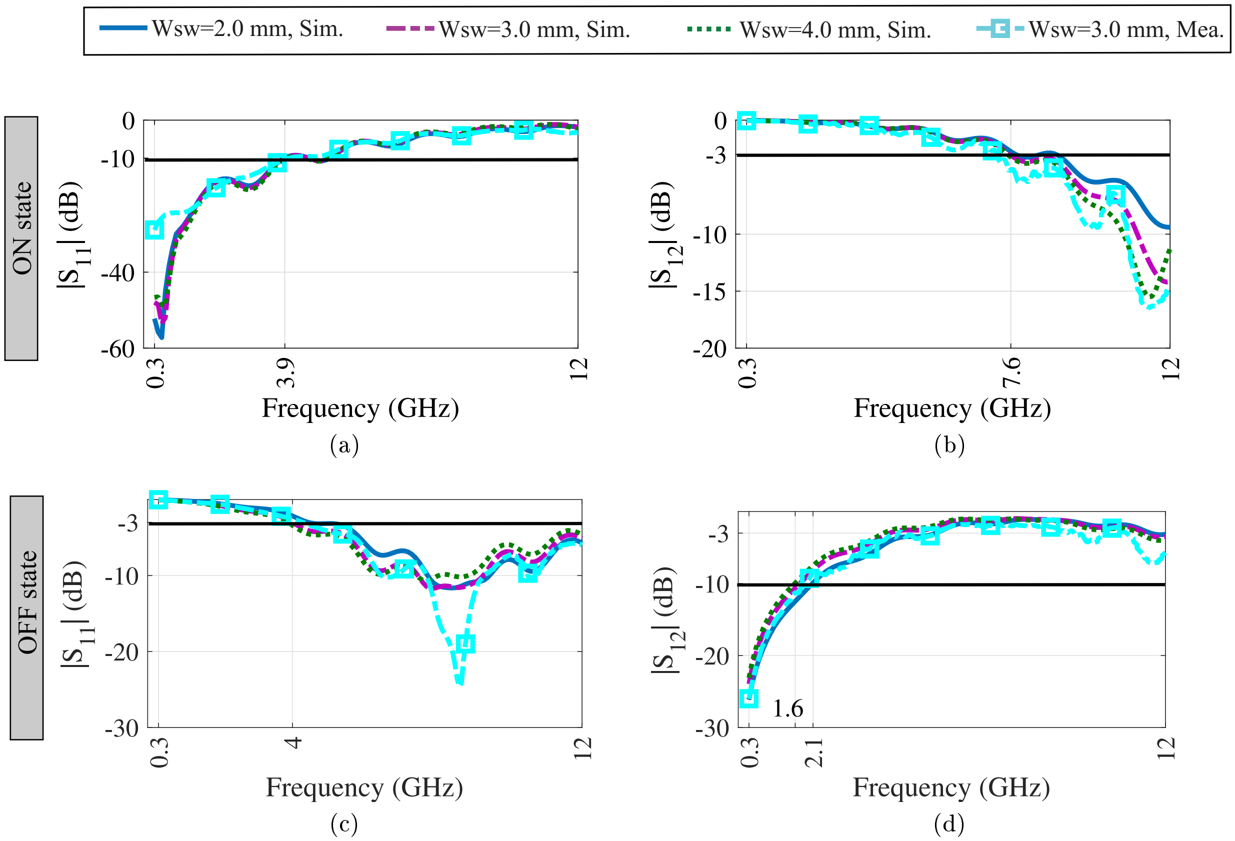

(a)
(b)
(c)
(d)

Figure 2.7. HFSS simulation and measurement results of the traditional SSwSC for $w_{sw} = 2.0$ mm, 3.0 mm, and 4.0 mm (a) $|S_{11}|$ for ON state, (b) $|S_{12}|$ for ON state, (c) $|S_{11}|$ for OFF state, and (d) $|S_{12}|$ for OFF state.

3. NEW EMBODIMENTS OF STATIC FIELD MICRO-PARTICLE COMPONENTS (SFM-PCS)

In the previous chapter, the effects of the physical characteristics of the switch were formulated. Table I compares the performance of both ON and OFF states with respect to the dielectric constant ϵ_{sw}, height h_{sw}, width w_{sw}, and length l_{sw} of the switch. As can be seen from this table, there is a trade-off between the OFF and ON states for the height of the switch. In other words, while reducing the height increases the frequency bandwidth of the ON state, it degrades the frequency band of the OFF state. In addition, due to fabrication limitations, reducing the length and the width of the switch in order to lower the isolation loss for the desired frequency range in not possible. Therefore, developing new techniques that can either improve the frequency bandwidth of both states or improve the frequency bandwidths of one state without degrading the performance of the other one is a must. Hence, in this chapter, two novel techniques, Asymmetric Copper (AC) and Double Switch (DSw) will be introduced. By employing these methods, the frequency bandwidth of the SFM-PC can increase up to 7.0 GHz, several times of the previously reported values.

Table 3.1. Effects of the physical characteristics of the SFM-PC switch on both ON and OFF states.

	Physical characteristic	Value	ON state	OFF state
Switch	dielectric constant (ϵ_{sw})	high		
		low		√
	height (h_{sw})	high		√
		low	√	
	width (w_{sw})	high		
		low		√
	length (l_{sw})	high		
		low	√	√

√ symbol was used to show the improvement in the frequency bandwidth.

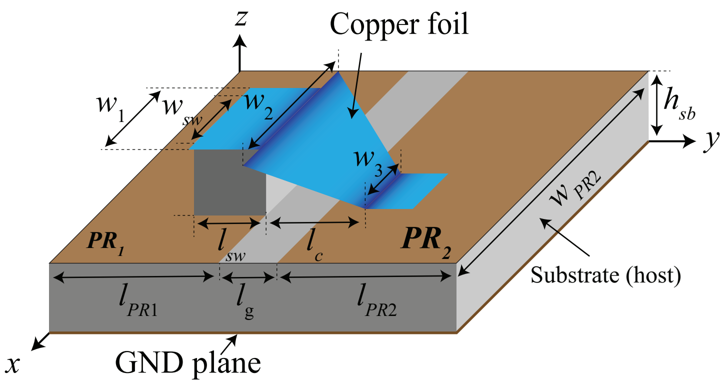

Figure 3.1. Structure of the Single Switch Asymmetric Copper (SSwAC).

3.1. Single Switch Asymmetric Copper (SSwAC)

Fig. 3.1 shows the proposed Asymmetric Copper (AC) technique applied to a single switch in order to improve the frequency bandwidth of the switch for the ON state without compromising the performance of the OFF state. Unlike the traditional SFM-PC, in this method, an asymmetric copper foil is used to connect the top side of the switch to PR_2 of the host. In other words, the widths of the copper foil, w_1 and w_2, could have different values from the width of the switch, w_{sw}. It will be shown that by properly adjusting the widths of the copper foil, the reflection coefficient can be reduced considerably resulting in increased frequency bandwidth for the ON state.

3.1.1. ON state

As discussed in the previous chapter, because of impedance mismatch, some part of the signal reflects at the boundaries between different regions, reducing the feedforward transmission coefficient, $|S_{12}|$, and increasing the voltage reflection coefficient, $|S_{11}|$. Similar to the traditional structure, the Single Switch Asymmetric Copper (SSwAC) structure creates two regions called 1 and 2 with characteristic impedances of $Z_{0,1}$ and $Z_{0,2}$, respectively.

3.1.1.1. Region 1

As $w_1 \geq w_{sw}$, air covers the $w_y = w_1 - w_{sw}$ part of the copper foil in the first region. Using the methodology described for the traditional Single Switch Symmetric Copper (SSwSC), the capacitance per unit length and the inductance per unit length in the first region can be calculated from the following equations:

$$C_1 = \frac{\epsilon_{sw} f(w_{sw}, h_{sw}) + 2f(w_y, h_{sw})}{\epsilon_{sw} f(w_{sw}, h_{sw}) + 2f(w_y, h_{sw}) + \epsilon_{sb} f(w_{sw} + 2w_y, h_{sb})} \frac{f(w_{sw} + 2w_y, h_{sb})}{f(w_t, h_{sb})} C_0 \tag{3.1}$$

and

$$L_1 = \frac{120\pi}{f(w_{sw} + 2w_y, h_{sb} + h_{sw})c}, \tag{3.2}$$

where ϵ_{sw} is the dielectric constant of the switch, w_{sw} is the width of the switch, h_{sw} is the height of the switch, h_{sb} is the height of the substrate, and w_t is the width of the trace. Using (3.1) and (3.2), the characteristic impedance in the first region can be obtained from

$$Z_{0,1} = \sqrt{\frac{L_1}{C_1}} = Z_0 D_1, \tag{3.3}$$

in which the coefficient D_1 is from (3.4).

$$D_1 = \sqrt{\frac{f^2(w_t, h_{sb})\Big(\epsilon_{sw} f(w_{sw}, h_{sw}) + 2f(w_y, h_{sw}) + \epsilon_{sb} f(w_{sw} + 2w_y, h_{sb})}{f(w_{sw} + 2w_y, h_{sb}) f(w_{sw} + 2w_y, h_{sb} + h_{sw})\Big(\epsilon_{sw} f(w_{sw}, h_{sw}) + 2f(w_y, h_{sw})\Big)}} \tag{3.4}$$

3.1.1.2. Region 2

Assuming the width of the copper foil in the kth segment of the second region is w_2^k, the capacitance per unit length, inductance per unit length, and the characteristic impedance in this region can be calculated from the equations shown below.

$$C_2^k = \frac{f(w_2^k, h_{sb}) f(w_2^k, h_2^k)}{f(w_t, h_{sb})\Big(f(w_2^k, h_2^k) + \epsilon_{sb} f(w_2^k, h_{sb})\Big)} C_0, \tag{3.5}$$

$$L_2^k = \frac{f(w_t, h_{sb})}{f(w_2^k, h_2^k + h_{sb})} L_0, \tag{3.6}$$

and

$$Z_2^k = Z_0 D_2^k, \tag{3.7}$$

where

$$h_2^k = \frac{N - k + 2}{N} h_{sw} \tag{3.8}$$

and

$$D_2^k = \sqrt{\frac{f^2(w_t, h_{sb})\Big(f(w_2^k, h_2^k) + \epsilon_{sb} f(w_2^k, h_{sb})\Big)}{f(w_2^k, h_{sb}) f(w_2^k, h_2^k) f(w_2^k, h_2^k + h_{sb})}}. \tag{3.9}$$

Using the characteristic impedances, the voltage reflection coefficient for the Single Switch Asymmetric Copper (SSwAC) can be written as

$$\Gamma_1^{SSwAC} = \frac{\Gamma_1^{SSwAC}|_{Num.}}{\Gamma_1^{SSwAC}|_{Den.}}, \tag{3.10}$$

in which its numerator and denominator are given by

$$\begin{aligned}\Gamma_1^{SSwAC}|_{Num.} = {} & \sum_{i=1}^{N+1} j\Big(\prod_{b_p \in B_i^1} D_{b_p}\Big)\Big(\prod_{a_q \in A_i^1} \tan(\beta_{a_q} l_{a_q})\Big)\Big((D_{a_q})^2 - 1\Big) \\ & + \sum_{m=2}^{N}\Big(\sum_{i=1}^{\binom{N+1}{m}} j^m \big(\prod_{b_p \in B_i^m} D_{b_p}\big)\big(\prod_{a_q \in A_i^m} \tan(\beta_{a_q} l_{a_q})\big)\big(\prod_{\substack{q\ odd \\ a_q \in A_i^m}} (D_{a_q})^2 - \prod_{\substack{q\ even \\ a_q \in A_i^m}} (D_{a_q})^2\big)\Big) \\ & + j^{N+1}\big(\prod_{a_q \in A_i^{N+1}} \tan(\beta_{a_q} l_{a_q})\big)\big(\prod_{\substack{q\ odd \\ a_q \in A_i^{N+1}}} (D_{a_q})^2 - \prod_{\substack{q\ even \\ a_q \in A_i^{N+1}}} (D_{a_q})^2\big)\end{aligned} \tag{3.11}$$

$$\begin{aligned}\Gamma_1^{SSwAC}|_{Den.} = {} & 2 \times \big(\prod_{i \in U} D_i\big) + \sum_{i=1}^{N+1} j\Big(\prod_{b_p \in B_i^1} D_{b_p}\Big)\Big(\prod_{a_q \in A_i^1} \tan(\beta_{a_q} l_{a_q})\Big)\Big((D_{a_q})^2 + 1\Big) \\ & + \sum_{m=2}^{N}\Big(\sum_{i=1}^{\binom{N+1}{m}} j^m \big(\prod_{b_p \in B_i^m} D_{b_p}\big)\big(\prod_{a_q \in A_i^m} \tan(\beta_{a_q} l_{a_q})\big)\big(\prod_{\substack{q\ odd \\ a_q \in A_i^m}} (D_{a_q})^2 + \prod_{\substack{q\ even \\ a_q \in A_i^m}} (D_{a_q})^2\big)\Big) \\ & + j^{N+1}\big(\prod_{a_q \in A_i^{N+1}} \tan(\beta_{a_q} l_{a_q})\big)\big(\prod_{\substack{q\ odd \\ a_q \in A_i^{N+1}}} (D_{a_q})^2 + \prod_{\substack{q\ even \\ a_q \in A_i^{N+1}}} (D_{a_q})^2\big),\end{aligned} \tag{3.12}$$

where

$\Big\{A_i^m\Big\}$: is the collection of $i(=\binom{N+1}{m})$ subsets of $U = \{1, 2, \cdots, N+1\}$ with size m

$A_i^m = \Big\{a_1, \cdots, a_q, \cdots, a_m\Big\}$ in which $a_q < a_{q+1}$

$\Big\{B_i^m\Big\}$: is the collection of i subsets of $U = \{1, 2, \cdots, N+1\}$ with size $N+1-m$

$B_i^m = \Big\{b_1, \cdots, b_p, \cdots, b_{N+1-m}\Big\}$ such that $B_i^m \cup A_i^m = U$ and $B_i^m \cap A_i^m = \varnothing$

While the formulas for the reflection coefficient of the SSwAC is the same as the SSwSC, the ratio of the characteristic impedance of each region to that of the host ($D_i = \frac{Z_{0,i}}{Z_0}$) is different for them. In SSwAC, the D_i's are dependent on w_w and w_2^k which are unknown and their values should be adjusted to reduce the reflection coefficient.

3.1.2. OFF state

The circuit equivalent of SSwAC for the OFF state is the same as the traditional SSwSC. For this circuit, $C_{coupling} = C_{sw} + C_h + C_f$ where C_f is the fringing capacitance between the copper foil and PR_2. Because the size of the copper foil of SSwAC is larger compared to the traditional one, it might cause a slight reduction in the frequency bandwidth of the OFF state.

3.2. Double Switch Symmetric Copper (DSwSC)

For improving the frequency bandwidth of the OFF state, the Double Switch (DSw) technique was developed. Fig. 3.2 illustrates the Double Switch Symmetric Copper SFM-PC. It consists of two SFM-PC switches with the same physical characteristic (ϵ_{sw}, h_{sw}, w_{sw}, and l_{sw}) placed on both edges of the gap; connected together using a symmetric copper foil with the widths of $w_1 = w_2 = w_3$. Each of these switches was filled with the same amount of the micron-sized silver coated particles.

3.2.1. ON state

The main signal path for the DSwSC technique for the ON state is illustrated by a green arrow in Fig. 3.2(b). Due to the embodiment of the switches, three regions called 1, 2, and 3 were created.

3.2.1.1. Region 1 and 3

The physical characteristics of both switches are the same; hence, the first and third regions have equal capacitance and inductance per unit length, resulting in the same characteristic impedance values, in other words, $Z_{0,1} = Z_{0,3}$. The capacitance per unit length, the inductance

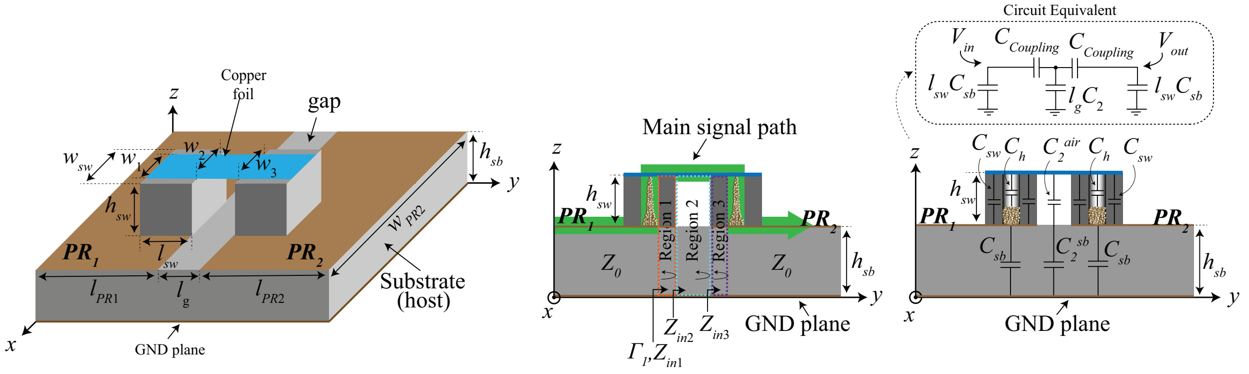

(a) (b) (c)

Figure 3.2. Double Switch Symmetric Copper (DSwSC) (a) structure, (b) signal path for the ON state, and (c) circuit equivalent for OFF state.

per unit length, and the characteristic impedance in these regions can be calculated from equations shown below;

$$C_1 = \frac{C_1^{sw} C_1^{sb}}{C_1^{sw} + C_1^{sb}} = \frac{\epsilon_{sw} f(w_{sw}, h_{sw}) f(w_{sw}, h_{sb})}{f(w_t, h_{sb})\Big(\epsilon_{sw} f(w_{sw}, h_{sw}) + \epsilon_{sb} f(w_{sw}, h_{sb})\Big)} C_0, \tag{3.13}$$

$$L_1 = \frac{120\pi}{f(w_{sw}, h_{sb} + h_{sw})c} = \frac{f(w_t, h_{sb})}{f(w_{sw}, h_{sb} + h_{sw})} L_0, \tag{3.14}$$

and

$$Z_{0,1} = Z_{0,3} = \sqrt{\frac{L_1}{C_1}} = Z_0 \times D_1, \tag{3.15}$$

where

$$D_1 = \sqrt{\frac{f^2(w_t, h_{sb})\Big(\epsilon_{sw} f(w_{sw}, h_{sw}) + \epsilon_{sb} f(w_{sw}, h_{sb})\Big)}{\epsilon_{sw} f(w_{sw}, h_{sw}) f(w_{sw}, h_{sb}) f(w_{sw}, h_{sb} + h_{sw})}} \tag{3.16}$$

3.2.1.2. Region 2

For the second region of the Double Switch Symmetric Copper (DSwSC), C_2, L_2, and $Z_{0,2}$ can be found from the following equations.

$$C_2 = \frac{C_1^{air} C_1^{sb}}{C_1^{air} + C_1^{sb}} = \frac{f(w_{sw}, h_{sw}) f(w_{sw}, h_{sb})}{f(w_t, h_{sb})\Big(f(w_{sw}, h_{sw}) + \epsilon_{sb} f(w_{sw}, h_{sb})\Big)} C_0, \tag{3.17}$$

$$L_2 = \frac{120\pi}{f(w_{sw}, h_{sb} + h_{sw})c} = \frac{f(w_t, h_{sb})}{f(w_{sw}, h_{sb} + h_{sw})} L_0, \tag{3.18}$$

and

$$Z_{0,2} = \sqrt{\frac{L_2}{C_2}} = Z_0 \times D_2, \tag{3.19}$$

in which the coefficient D_2 is given by (3.20).

$$D_2 = \sqrt{\frac{f^2(w_t, h_{sb})\Big(f(w_{sw}, h_{sw}) + \epsilon_{sb} f(w_{sw}, h_{sb})}{f(w_{sw}, h_{sw}) f(w_{sw}, h_{sb}) f(w_{sw}, h_{sb} + h_{sw})}}. \tag{3.20}$$

Using $Z_{0,1}$ and $Z_{0,2}$, the voltage reflection coefficient for the Double Switch Symmetric Copper (DSwSC) can be calculated from the following equation in which its numerator and denominator are given by (3.22) and (3.23), respectively.

$$\Gamma_1^{DSwSC} = \frac{\Gamma_1^{DSwSC}|_{Num.}}{\Gamma_1^{DSwSC}|_{Den.}} \tag{3.21}$$

$$\begin{aligned}\Gamma_1^{DSwSC}|_{Num.} &= 2jD_1D_2\tan(\beta_1 l_1)\big((D_1)^2-1\big) + j(D_1)^2\tan(\beta_2 l_g)\big((D_2)^2-1\big)\\ &\quad - j\big(tan(\beta_1 l_1)\big)^2\tan(\beta_2 l_g)\big((D_1)^4-(D_2)^2\big) \qquad (3.22)\\ \Gamma_1^{DSwSC}|_{Den.} &= 2jD_1D_2\tan(\beta_1 l_1)\big((D_1)^2+1\big) + j(D_1)^2\tan(\beta_2 l_g)\big((D_2)^2+1\big)\\ &\quad - 2D_1\tan(\beta_1 l_1)\tan(\beta_2 l_g)\big((D_1)^2+(D_2)^2\big) + 2(D_1)^2D_2\Big(1-(\tan(\beta_1 l_1))^2\Big)\\ &\quad - j\big(\tan(\beta_1 l_1)\big)^2\tan(\beta_2 l_g)\big((D_1)^4+(D_2)^2\big). \qquad (3.23)\end{aligned}$$

3.2.1.3. OFF state

In order to evaluate the effects of the proposed Double Switch technique on the OFF state, the equivalent circuit illustrated in Fig. 3.2(c) was used. The relationship between the output and input can be obtained as

$$V_{out}^{DSwSC} = \frac{C_{coupling}}{C_{coupling} + 2C_{sb}l_{sw} + C_2 l_g\big(1+\frac{C_{sb}l_{sw}}{C_{coupling}}\big)} \times V_{in}, \tag{3.24}$$

where l_g is the length of the gap and l_{sw} is the length of the switch. Comparing (3.24) to that for the traditional SSwSC, it can be concluded that the Double Switch (DSw) technique reduces the output coupling voltage and consequently improves the frequency bandwidth of the OFF state.

3.3. Double Switch Asymmetric Copper (DSwAC)

Combining both Asymmetric Copper (AC) and Double Switch (DSw) techniques results in Double Switch Asymmetric Copper (DSwAC) structure illustrated in Fig. 3.3. Unlike the DSwSC in which $w_1 = w_2 = w_3$, in this technique the widths of the copper foil are different from the width of the switch w_{sw}. Both ON and OFF states of DSwAC are evaluated separately in the following subsections.

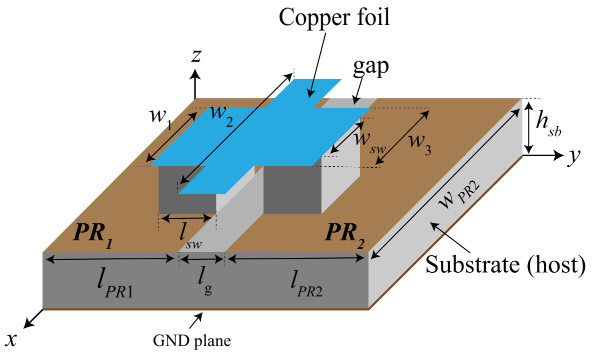

Figure 3.3. Structure of the Double Switch Asymmetric Copper (DSwAC).

3.3.1. ON state

Similar to the Double Switch Symmetric Copper, the embodiment of the switch on the host creates three regions called 1, 2, and 3. As both switches have the same physical characteristics and filled with equal amount of micron-sized particles, the total capacitance per unit length, the inductance per unit length, and the characteristic impedance in the first and third regions are the same. These parameters can be found as follows:

$$C_1 = \frac{\epsilon_{sw} f(w_{sw}, h_{sw}) + 2f(w_y, h_{sw})}{\epsilon_{sw} f(w_{sw}, h_{sw}) + 2f(w_y, h_{sw}) + \epsilon_{sb} f(w_{sw} + 2w_y, h_{sb})} \frac{f(w_{sw} + 2w_y, h_{sb})}{f(w_t, h_{sb})} C_0, \tag{3.25}$$

$$L_1 = \frac{120\pi}{f(w_{sw} + 2w_y, h_{sb} + h_{sw})c}, \tag{3.26}$$

and

$$Z_{0,1} = \sqrt{\frac{L_1}{C_1}} = Z_0 D_1, \tag{3.27}$$

in which the coefficient D_1 is given by (3.28).

$$D_1 = \sqrt{\frac{f^2(w_t, h_{sb})\Big(\epsilon_{sw} f(w_{sw}, h_{sw}) + 2f(w_y, h_{sw}) + \epsilon_{sb} f(w_{sw} + 2w_y, h_{sb})\Big)}{f(w_{sw} + 2w_y, h_{sb}) f(w_{sw} + 2w_y, h_{sb} + h_{sw})\Big(\epsilon_{sw} f(w_{sw}, h_{sw}) + 2f(w_y, h_{sw})\Big)}} \tag{3.28}$$

For the second region which has a fixed width along the gap, the capacitance per unit length C_2, the inductance per unit length L_2, and the characteristic impedance $Z_{0,2}$ are given by

$$C_2 = \frac{f(w_2, h_{sw})}{f(w_2, h_{sw}) + \epsilon_{sb} f(w_2, h_{sb})} \frac{f(w_2, h_{sb})}{f(w_t, h_{sb})} C_0, \tag{3.29}$$

$$L_2 = \frac{120\pi}{f(w_2, h_{sb} + h_{sw})c} = \frac{f(w_t, h_{sb})}{f(w_2, h_{sb} + h_{sw})} L_0, \tag{3.30}$$

and

$$Z_{0,2} = Z_0 D_2, \tag{3.31}$$

where

$$D_2 = \sqrt{\frac{f^2(w_t, h_{sb})\Big(f(w_2, h_{sw}) + \epsilon_{sb} f(w_2, h_{sb})\Big)}{f(w_2, h_{sw}) f(w_2, h_{sb}) f(w_2, h_{sb} + h_{sw})}}. \tag{3.32}$$

For the DSwAC, the voltage reflection coefficient, Γ_1^{DSwAC}, can be defined by (3.33) in which its numerator and denominator are represented by (3.34) and (3.35), respectively.

$$\Gamma_1^{DSwAC} = \frac{\Gamma_1^{DSwAC}|_{Num.}}{\Gamma_1^{DSwAC}|_{Den.}} \tag{3.33}$$

$$\begin{aligned} \Gamma_1^{DSwAC}|_{Num.} &= 2jD_1D_2 \tan(\beta_1 l_1)\big((D_1)^2 - 1\big) + j(D_1)^2 \tan(\beta_2 l_g)\big((D_2)^2 - 1\big) \\ &\quad - j\big(tan(\beta_1 l_1)\big)^2 \tan(\beta_2 l_g)\big((D_1)^4 - (D_2)^2\big) \qquad (3.34) \\ \Gamma_1^{DSwAC}|_{Den.} &= 2jD_1D_2 \tan(\beta_1 l_1)\big((D_1)^2 + 1\big) + j(D_1)^2 \tan(\beta_2 l_g)\big((D_2)^2 + 1\big) \\ &\quad - 2D_1 \tan(\beta_1 l_1) \tan(\beta_2 l_g)\big((D_1)^2 + (D_2)^2\big) + 2(D_1)^2 D_2 \Big(1 - (\tan(\beta_1 l_1))^2\Big) \\ &\quad - j\big(\tan(\beta_1 l_1)\big)^2 \tan(\beta_2 l_g)\big((D_1)^4 + (D_2)^2\big). \qquad (3.35) \end{aligned}$$

For the reflection coefficient to be zero, D_1 and D_2 should go to unity. By solving $D_1 = 1$ and $D_2 = 1$, the widths of the copper foil, w_1 and w_2 can be obtained.

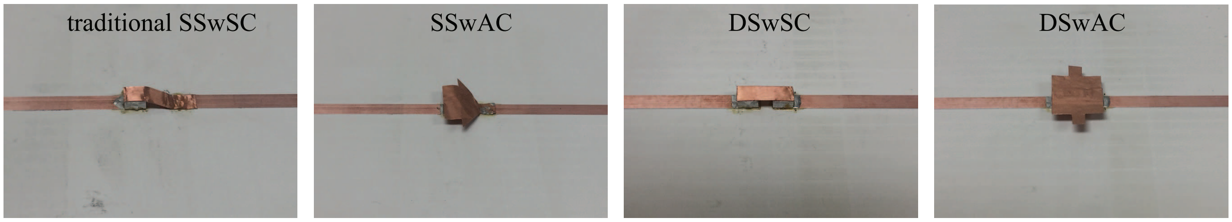

Figure 3.4. Fabricated prototypes for traditional SSwSC, SSwAC, DSwSC, and DSwAC.

3.3.2. OFF state

The relationship between input and output of Double Switch Asymmetric Copper(DSwAC) can be derived from

$$V_{out}^{DSwAC} = \frac{C_{coupling}}{C_{coupling} + 2C_{sb}l_{sw} + C_2 l_g(1 + \frac{C_{sb}l_{sw}}{C_{coupling}})} \times V_{in}. \tag{3.26}$$

While V_{out}/V_{in} for both DSwAC and DSwSC seems similar, the denominator of V_{out}^{DSwAC}/V_{in} is larger because of C_2. This implies higher frequency bandwidth of DSwAC for the OFF state.

3.4. Simulation and measurement results

The effects of the proposed Asymmetric Copper (AC) and the Double Switch (DSw) techniques on the frequency bandwidth of both ON and OFF states were evaluated using the HFSS simulation as well as by measurements in the anechoic chamber. All the switches for different methodologies were designed from Rogers TMM4 with the height 1.524 mm, length 3.0 mm, width 3.0 mm, and cavity radius 0.5 mm. Fig. 3.4 shows the fabricated prototypes embedded on a discontinuous host transmission line (TL) with height 1.524 mm and dimension 80 mm × 80 mm. The simulation and the measurement results were illustrated in Figs. 3.5, 3.6, 3.7, and 3.8 for the traditional Single Switch Symmetric Copper (SSwAC), Single Switch Asymmetric Copper (SSwAC), Double Switch Symmetric Copper (DSwSC), and Double Switch Asymmetric Copper (DSwAC). As expected, the Asymmetric Copper (AC) technique increase the frequency bandwidth of the ON state, the Double Switch (DSw) improve the frequency bandwidths of the OFF state considerably.

3.5. Conclusion

Novel Asymmetric Copper and Double Switch (DSw) techniques to increase the frequency bandwidth of the Static Field Micro-Particle Component (SFM-PC) were proposed and analyzed

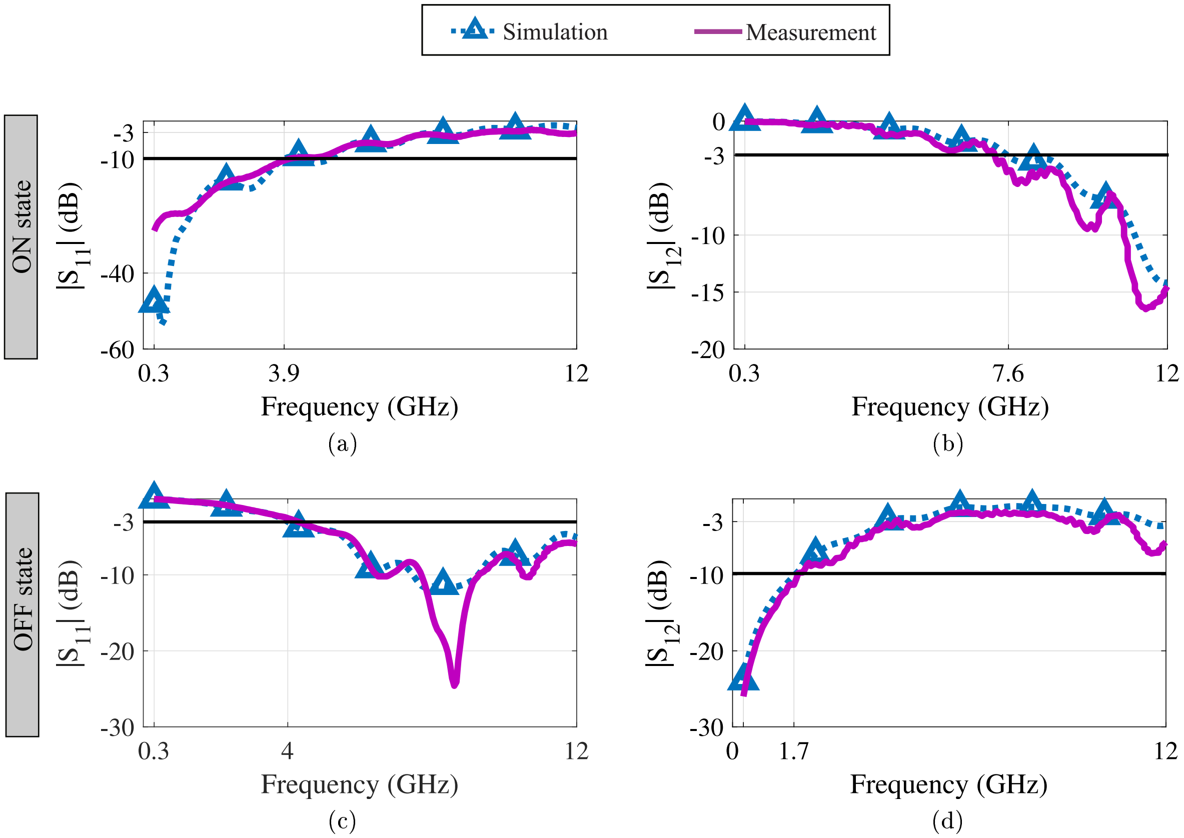

Figure 3.5. HFSS simulation and measurement results of the traditional SSwSC (a) $|S_{11}|$ for ON state, (b) $|S_{12}|$ for ON state, (c) $|S_{11}|$ for OFF state, and (d) $|S_{12}|$ for OFF state.

thoroughly. HFSS simulation and measurement results proved the effectiveness of the proposed methods and the accuracy of the presented analysis.

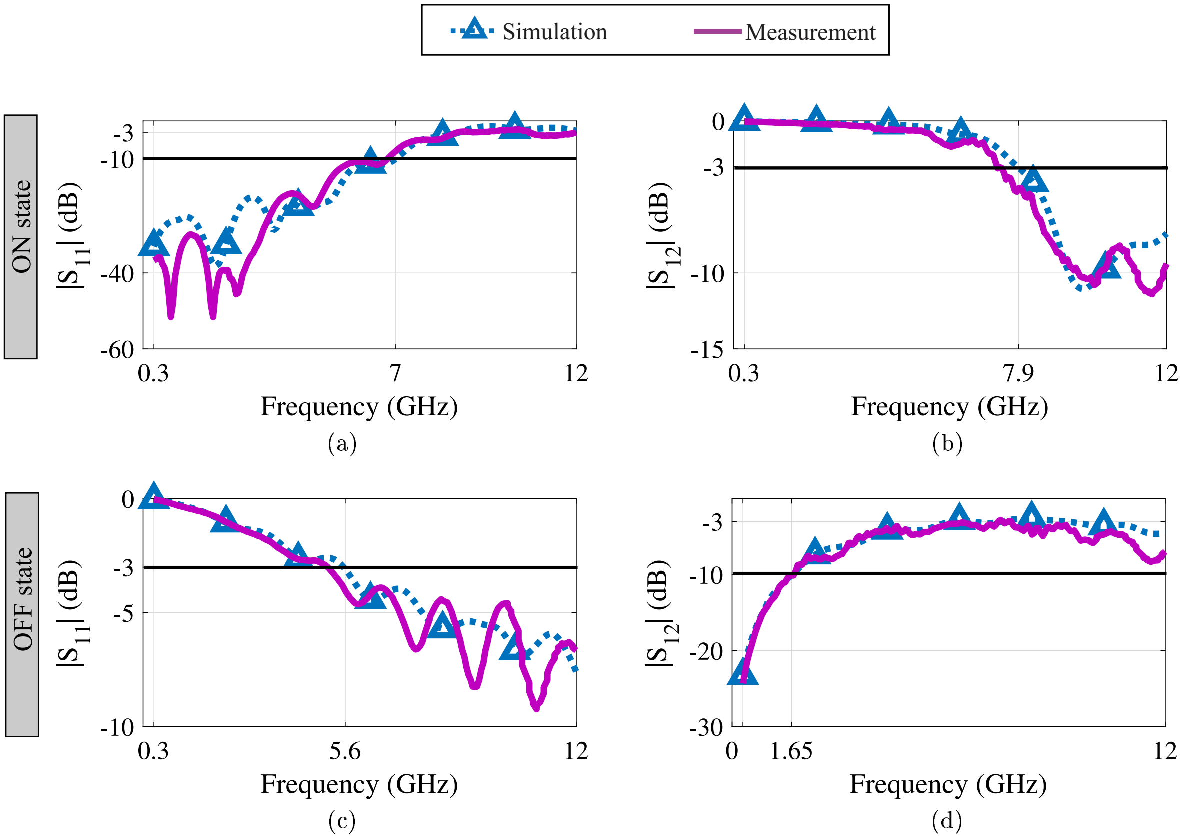

Figure 3.6. HFSS simulation and measurement results of the SSwAC (a) $|S_{11}|$ for ON state, (b) $|S_{12}|$ for ON state, (c) $|S_{11}|$ for OFF state, and (d) $|S_{12}|$ for OFF state.

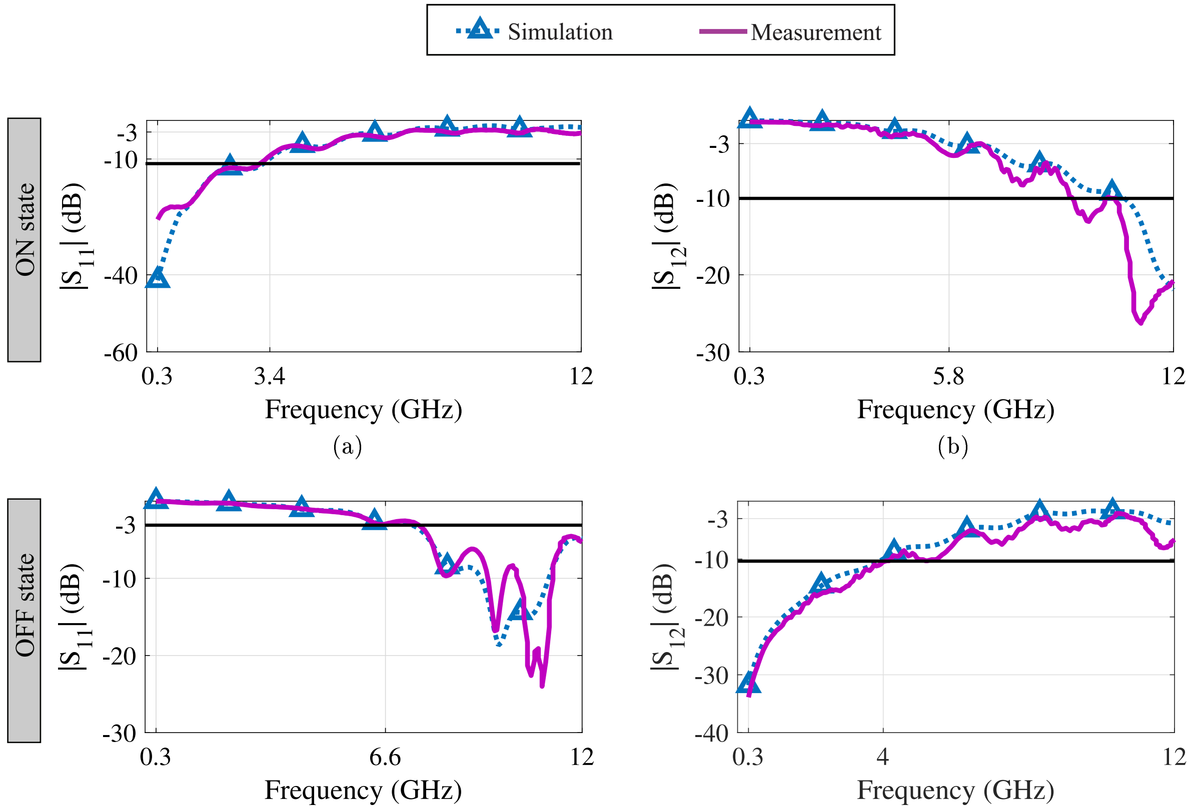

(a) (b) (c) (d)

Figure 3.7. HFSS simulation and measurement results of the DSwSC (a) $|S_{11}|$ for ON state, (b) $|S_{12}|$ for ON state, (c) $|S_{11}|$ for OFF state, and (d) $|S_{12}|$ for OFF state.

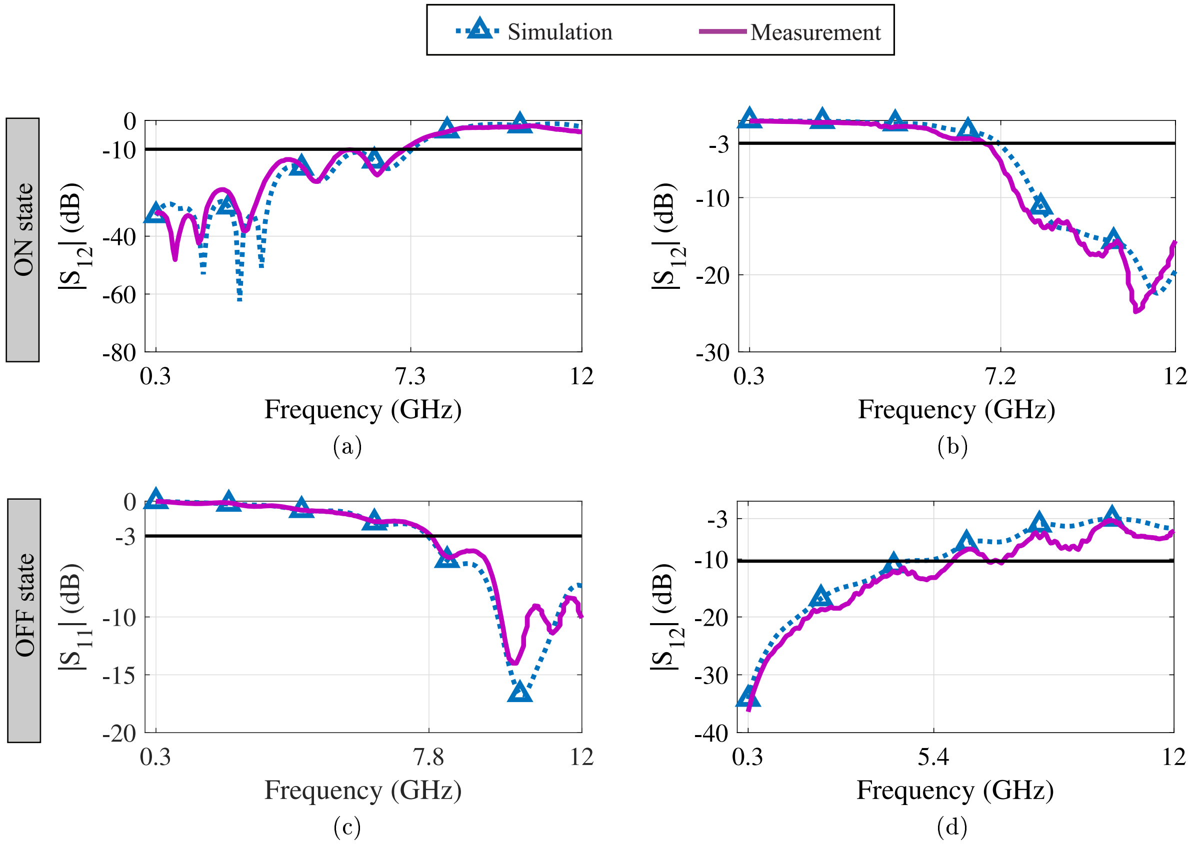

Figure 3.8. HFSS simulation and measurement results of the DSwAC (a) $|S_{11}|$ for ON state, (b) $|S_{12}|$ for ON state, (c) $|S_{11}|$ for OFF state, and (d) $|S_{12}|$ for OFF state.

4. ROTATABLE RF SWITCH BASED ON STATIC FIELD MICRO-PARTICLE COMPONENTS (SFM-PCS)

Due to the gravitational force, for a magnetic field applied from the $+z$-direction, rotating the switch θ degree around either x- or y-axes might lead to malfunction of the traditional particle-based switch. In other words, the top and bottom conducting plates may either be connected without the presence of the magnetic field or be disconnected in the presence of the static magnetic field. Fig. 4.1 illustrates the status of the micro particles inside the switch for both OFF and ON states for the rotation angle of 0° and 90°. When θ is 0°, the particles lie at the bottom of the cavity in the absence of magnetic field. Upon introducing the static magnetic field to the switch, the two conducting plates become connected through the stacked particles, acting as an RF switch in the ON state. However, for $\theta = 90°$, the switch might turn on when $\overline{H} = 0$ and be in the OFF state for $\overline{H} \neq 0$ as illustrated in Fig. 4.1(b).

By analyzing the switch, it can be realized that for a magnetic field applied from the $+z$-direction, as long as the rotation angle around either x- or y-axes stays within the ranges shown below, the switch will function correctly.

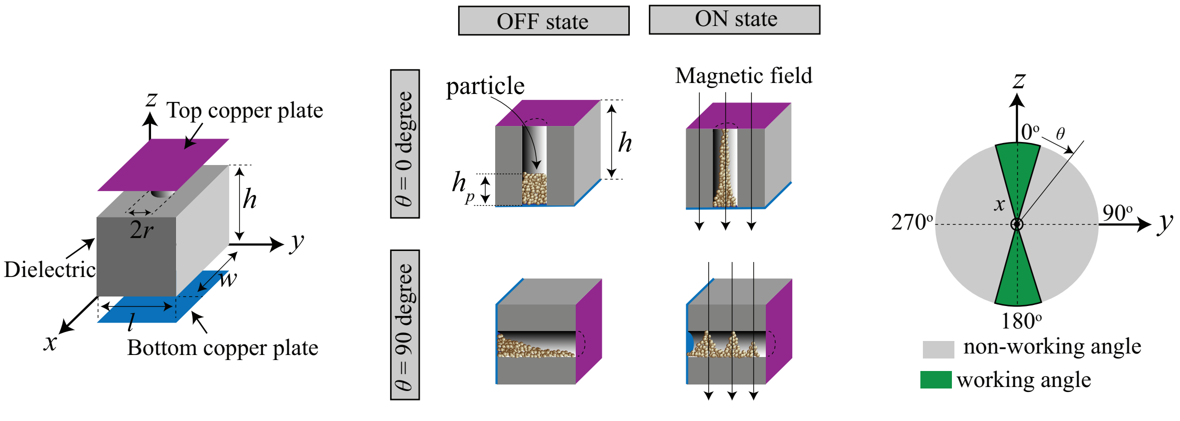

(a) (b) (c)

Figure 4.1. (a) Cross-sectional cut (zy plane) of the traditional SFM-PC (b) OFF and ON state for $\theta = 0$ and $\theta = 90°$ from the z-axis, and (c) rotation circle ('working' and 'non-working' angles).

$$\begin{cases} -\tan^{-1}(\alpha) & < \theta < +\tan^{-1}(\alpha) \\ 180-\tan^{-1}(\alpha) & < \theta < 180+\tan^{-1}(\alpha), \end{cases} \tag{4.1}$$

where $\alpha = \frac{2r}{h}$ and the positive values represent a clockwise rotation while the negative θ is used for counterclockwise rotation. Therefore, traditional SFM-PC is not a reliable technique to be used in rotatable RF systems. To address this challenge, in this chapter a novel rotatable structure that performs correctly while undergoing 360-degree rotations was developed.

4.1. Partial Rotatable Switch (P-RS)

Fig. 4.2 shows a rotatable structure based on the Static Field Micro-Particle Component (SFM-PC). It is a cube with cylindrical cavities of radius r drilled into the center of all its sides along x-, y-, and z-axes. The cube is made of dielectric material with the relative permittivity of ϵ_r and edge length of h. Squared copper foils with the length h' are placed on each cavity in order to enclose the particles inside the structure. Group of three copper foils that meet at a vertex of the cube creates the top and bottom copper plates. In other words, the arrangement is in such a way that the copper foils opposite to each other belong to different plates. It guarantees that when the structure undergoes any 90° rotation, a copper foil from the top and bottom plates always face each other.

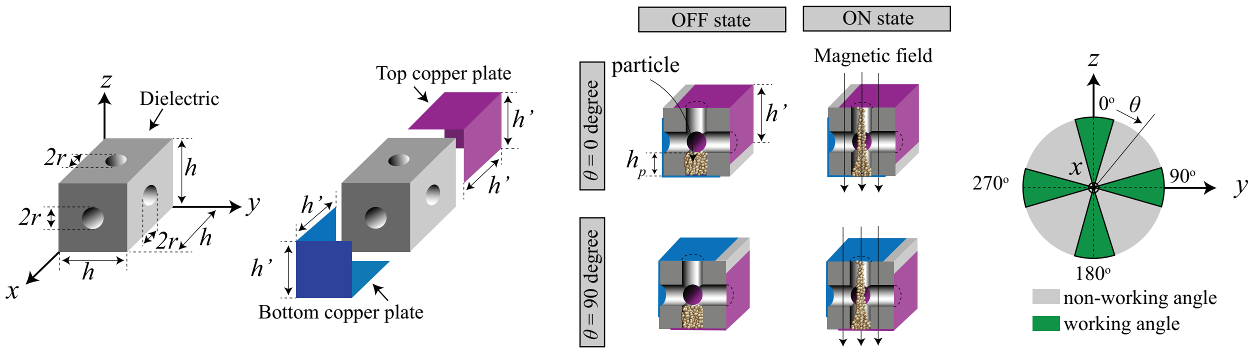

(a) (b) (c) (d)

Figure 4.2. Partial rotatable (P-RS) SFM-PC (a) structure, (b) top and bottom copper plates, (c) cross-sectional cut (zy-plane) of the ON and OFF states for $\theta = 0°$ and $\theta = 90°$ around the x-axis, and (d) rotation circle (‘working’ vs ‘non-working’ angles).

The functionality of the proposed structure can be described using the cross-sectional models illustrated in Fig. 4.2(c). When a static magnetic field is introduced in the $+z$-direction, the magnetic particles stack and align in columns in the direction of the field lines; connecting two copper foils which belong to the top and bottom plates, similar to the traditional SFM-PC. Conversely, when the magnetic field is removed, the columns collapse and disconnect the layers. When the switch undergoes certain rotations around one of the x- or y-axes, due to gravitational force the particles fall in the adjacent cavity; hence, the switch stays in the OFF state for the magnetic intensity of zero ($\overline{H}= 0$). On the other hand, in the presence of the static magnetic field ($\overline{H} \neq 0$), the particles form columns and the two conductive plates become connected, which consequently turning the rotated switch ON. As a result, the switch performs correctly while rotating any $90\pm\delta$ degrees (where δ is a small value); by staying in the OFF and ON states when the magnetic field is absent or present, respectively. The rotation angels in which the switch can perform reliably are given by

$$\begin{cases} -\tan^{-1}(\alpha) & < \theta < +\tan^{-1}(\alpha) \\ 90-\tan^{-1}(\alpha) & < \theta < 90+\tan^{-1}(\alpha) \\ 180-\tan^{-1}(\alpha) & < \theta < 180+\tan^{-1}(\alpha) \\ 270-\tan^{-1}(\alpha) & < \theta < 270+\tan^{-1}(\alpha), \end{cases} \tag{4.2}$$

where $\alpha = \frac{2r}{h}$.

Fig. 4.2(d) depicts the 'working angles' versus the 'non-working angles'. From equation (4.3), it can be realized that by increasing r with respect to h, the 'working angles' covers larger area; however, the distance between the cavity and edge of the cube is reduced. Therefore, for a fixed h, the size of the copper foil h' should be increased to enclose the micron-sized particles inside the cavity with a larger radius. This results in larger perpendicular capacitance between the top and bottom plates and degrades the frequency bandwidth for the OFF state. In addition, while for the traditional SFM-PC the height of particles can exceed the minimum required height without compromising the reliability of the design, $h_p \leq \frac{h-2r}{2}$ has to be satisfied for the proposed SFM-PC. Otherwise, because of the extra particles inside the channels, the switch might become ON when

$H = 0$. As can be concluded from the above discussion, this partial rotatable design covers certain angles and needs to be optimized in order to allow 360-degree rotation.

4.2. 360-degree Rotatable Switch (360-RS)

A 360-degree rotatable SFM-PC switch is illustrated in Fig. 4.3. It is a cube with the edge length equal to h in which two smaller cubes with the edge length of h'' are cut out of it in such a way that when the switch undergoes any rotation, there is always a cavity (opening) between the top and bottom plates. Similar to the partial rotatable SFM-PC shown in Fig. 4.2, each of the top and bottom copper plates is created from three squared copper foils with the edge length equal to h' such that $h' > h''$. As shown in Fig. 4.3(c), when $\overline{H} = 0$, the particles lie either on the top or bottom plates due to the gravitational force, causing the two copper plates to be disconnected. Because the area in which the particles can settle during OFF state is larger than that of partial rotatable (Fig. 4.2), a larger amount of the particles will not cause any reliability issues. When applying a static magnetic field, the top and bottom copper plates become connected through the stacked columns of micron-sized particles.

The rotation circle for the 360-degree SFM-PC is illustrated in Fig. 4.3(d); it shows that the 'working angle' covers the majority of the rotation circle. The rotation angles for reliable functionality of the switch can be found from (4.3) or (4.4) depending on the position of the switch and the direction of the rotation (clockwise or counterclockwise).

$$\begin{cases} -\tan^{-1}(\alpha) & < \theta < \ 90+\tan^{-1}(\alpha) \\ 180-\tan^{-1}(\alpha) & < \theta < \ 270(k+3)+\tan^{-1}(\alpha) \end{cases} \tag{4.3}$$

or

$$\begin{cases} 90-\tan^{-1}(\alpha) & < \theta < \ 180+\tan^{-1}(\alpha) \\ 270-\tan^{-1}(\alpha) & < \theta < \ +\tan^{-1}(\alpha), \end{cases} \tag{4.4}$$

where $\alpha = \frac{2h''-h}{h}$.

By analyzing these equations, it can be realized that while increasing h'' with respect to h reduces the 'non-working angles' portion, it results in a larger perpendicular capacitance between the edges of the top and bottom plates and degrades the frequency bandwidth of the OFF state.

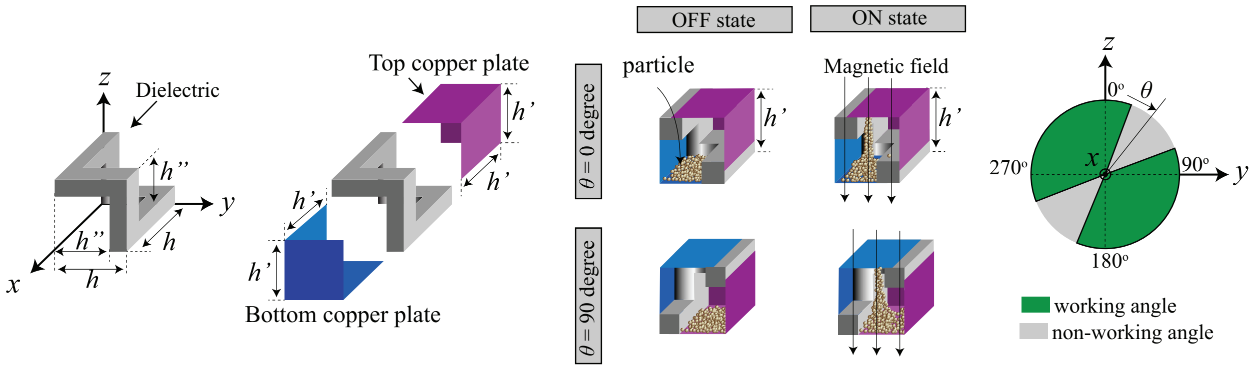

(a) (b) (c) (d)

Figure 4.3. A 360-degree rotatable SFM-PC (a) structure, (b) top and bottom copper plates, (c) cross-sectional cut (zy-plane) for both ON and OFF states when $\theta = 0°$ and $\theta = 90°$, and (d) rotation circle ('working' vs 'non-working' angles).

Alternatively, by combining two 360-degree switches, one is rotated -180° around the z-axis with respect to another, all the rotation angles from z-axis can be covered.

4.2.1. Capacitance between the top and bottom copper plates of 360-degree rotatable switch

The capacitance of the 360-degree rotatable switch can be estimated by considering a cube capacitor that is uniformly filled with a dielectric of relative permittivity ϵ_r and capped by two three-part metal plates as shown in Fig 4.3(b). The capacitance $C = \epsilon_0 \epsilon_r h \, \bar{c}(\frac{h'}{h})$ of the cube capacitor reflects its linear dimension h and the plate size h'. Note that $\bar{c}(\frac{h'}{h}) = 1$ for a parallel-plate capacitance (capacitance between the top and bottom copper plates of the traditional SFM-PC) with the plate area h^2 and plate-to-plate distance h. Using a finite element method in Mathematica, the function $\bar{c}(\frac{h'}{h})$ was numerically determined which is illustrated in Fig. 4.4 together with an approximate analytic expression $\bar{c}(\eta) = \pi\eta/[4(1-\eta)^{0.85}]$, where $\eta = \frac{h'}{h}$. The latter provides an excellent fit of the numerical data in the region $0 < \eta < 0.9$. We have obtained the linear part of the function $\bar{c}(\eta) = \pi\eta/4$, valid for $\eta \ll 1$, by using spheres of radius h' as an approximation for the two three-part metal plates. The denominator$(1-\eta)^{0.85}$ ensures a diverging capacitance for $\eta \to \infty$; the scaling exponent 0.85 represents a best fit of the numerical data. The capacitance of the cube capacitor can be accurately calculated from

$$C = \frac{\pi}{4} \frac{\epsilon_0 \epsilon_r h'}{(1 - h'/h)^{0.85}} \quad \text{when} \quad 0 < h'/h \leq 0.9. \tag{4.5}$$

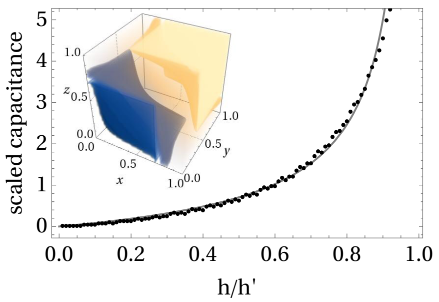

Figure 4.4. Scaled capacitance $\bar{c}(\eta) = C/(\epsilon_0 \epsilon_r h)$ as function of the ratio $\eta = h'/h$. For $\eta = 0.56$ the cube capacitor has the same capacitance as a parallel-plate capacitor. The inset shows a density plot of the scaled electrostatic potential within the cube capacitor for $\eta = 0.7$.

4.3. Simulation and measurement results

The functionality of the proposed rotatable switches was evaluated using both HFSS simulations and measurements in an anechoic chamber. A discontinuous transmission line (TL) made of Rogers TMM4 with $\epsilon_r = 4.7$, thickness 1.524 mm, and dimensions 80 mm × 80 mm was used as a host substrate to embed the SFM-PC switches. The traces of the TL have the widths of 2.79 mm and the gap between them was designed to be 2.0 mm in order to minimize the fringing capacitance between them and considering the effect of the parasitic capacitance introduced solely by the switch on the performance [14]. The TL was placed in the zy plane and rotated around the x-axis while the static magnetic field was being applied from the positive z-direction using a small permanent magnet. Figure 4.5 illustrates the schematic of the measurement setup and the embodiment of the 360-RS on the host TL made of Rogers TMM4.

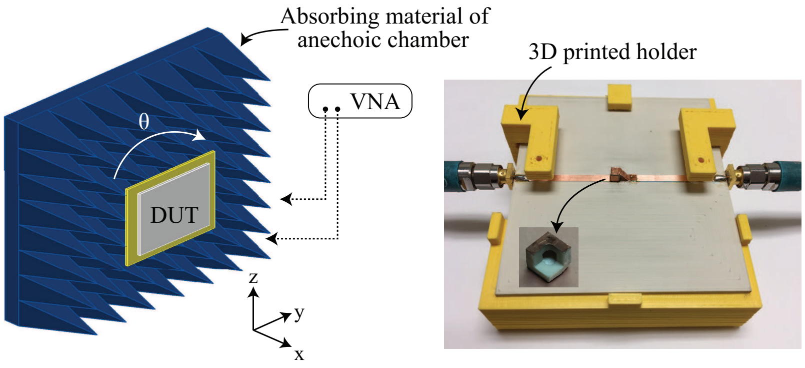

Figure 4.5. Measurement set-up and fabricated prototype of 360-RS made of Rogers TMM3 with h = 3.18 mm and h'' = 2.09 mm embedded on a TL.

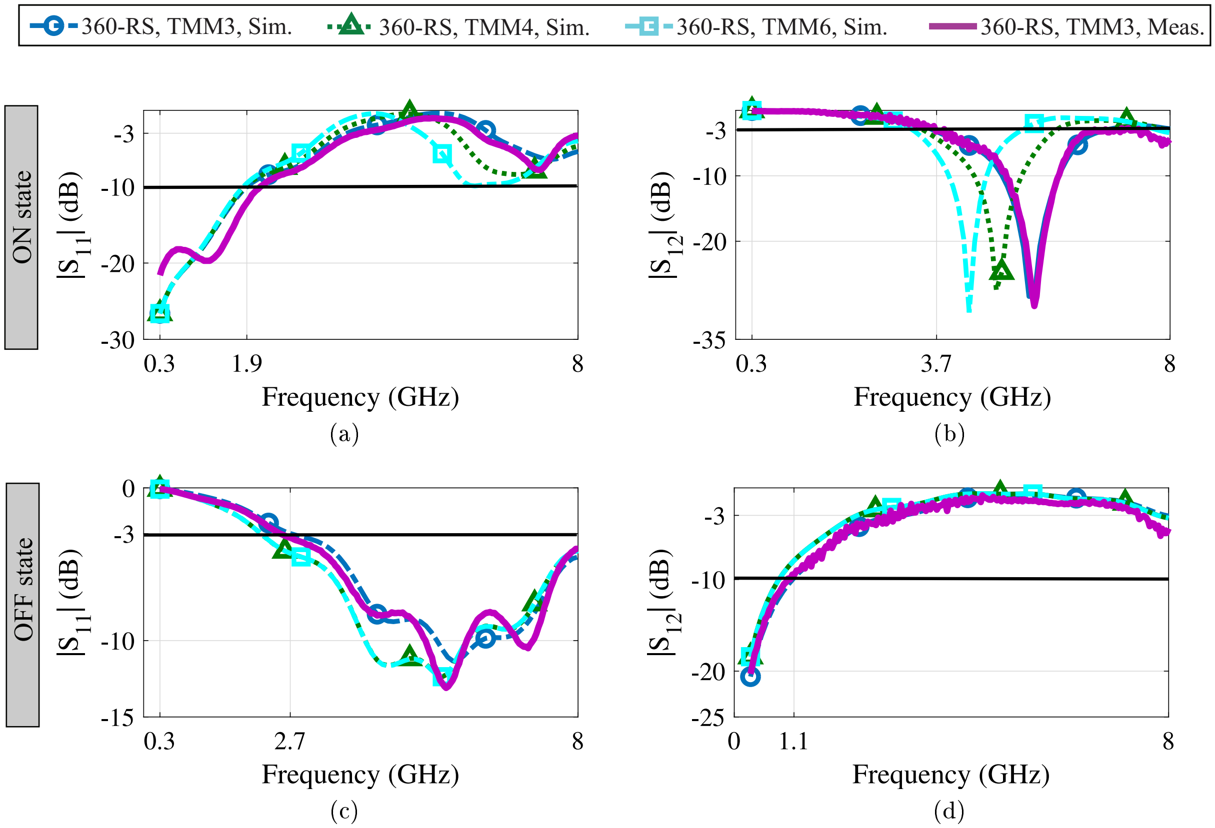

(a) (b) (c) (d)

Figure 4.6. HFSS simulation and measurement results for the 360-RS for various dielectric materiels including Rogers TMM3, Rogers TMM4, and Rogers TMM6 when $\theta = 0°$ (a) $|S_{11}|$ for ON state, (b) $|S_{12}|$ for ON state, (c) $|S_{11}|$ for OFF state, and (d) $|S_{12}|$ for OFF state.

The 360-degree rotatable SFM-PC switches were designed from Rogers TMM3 ($\epsilon = 3.45$ and $\tan\delta = 0.002$), TMM4 ($\epsilon = 4.7$ and $\tan\delta = 0.002$), and TMM6 ($\epsilon = 6.3$ and $\tan\delta = 0.0023$) with $h = 3.18$ mm and $h' = 2.09$ mm; these dimensions were chosen for ease of fabrication at NDSU Applied EM lab and can be scaled to smaller values. The copper foils with thickness of 0.5 oz and length of 2.7 mm were used to cover the cavities. Fig. 4.6 depicts the simulated and the measured results of both $|S_{11}|$ and $|S_{12}|$ for $\theta = 0°$ when the TL with embedded switch is in the xy plane. The static magnetic field was applied from the positive z direction using a small permanent magnet. As can be seen from the figure, while for the ON state, the -10 dB frequency of $|S_{11}|$ and the -3 dB frequency of $|S_{12}|$ for different dielectric materials are slightly different, the lower dielectric constant of Rogers TMM3 results in a higher frequency bandwidth for the OFF state compared to others.

A partial rotatable switch and a traditional SFM-PC made of Rogers TMM3 with edge length of 3.18 mm and cavity radius of 0.5 mm were also designed for comparison. The performance of the 360-RS, partial rotatable (P-RS), and traditional SFM-PC was evaluated for the rotation angle of 0°, 90°, 180°, and 270° from the z-axis when the transmission lines with the embedded switches were in the xy plane. Figures 4.7 and 4.8 show both $|S_{11}|$ and $|S_{12}|$ of all designs versus the frequency for the rotation angle of 0° and 90°, respectively. As can be seen from the figures, while both the 360-RS and P-RS work correctly for 0° and 90°, the traditional SFM-PC fails while undergoing a 90° rotation. In other words, the traditional switch turns ON when it should stay OFF ($\overline{H}= 0$) and becomes OFF in the presence of the static magnetic field ($\overline{H} \neq 0$). Additionally, while the frequency bandwidth of all designs is almost the same for the ON state, the frequency bandwidth of the traditional SFM-PC for the OFF state is higher compared to the rotatable structures. The lower frequency bandwidth of the rotatable structure is the result of larger coupling capacitance between its plates; as can be seen from Fig. 4.4, when $\eta = \frac{h'}{h} = 0.85$, $\bar{c}(\eta)$ of the cube capacitance is around 3 while for the parallel-plate capacitance $\bar{c}(\eta) = 1$.

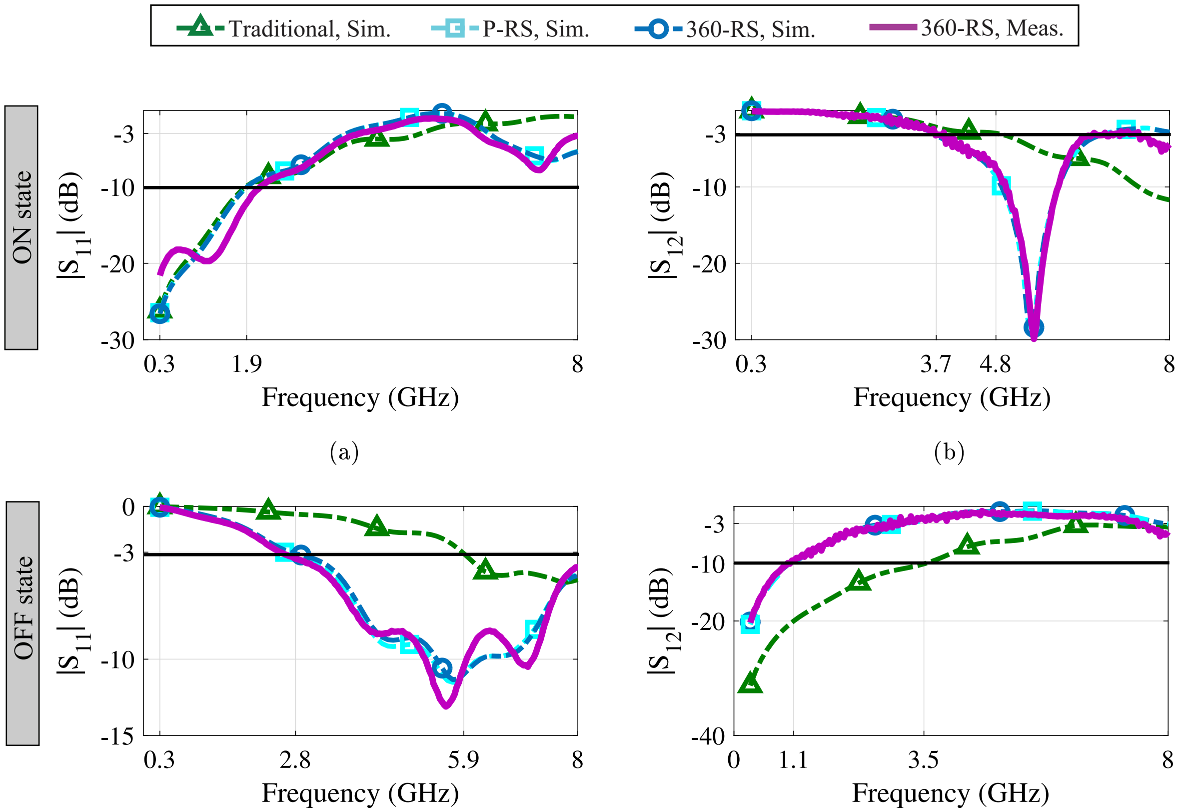

(a) (b)

(c) (d)

Figure 4.7. Simulation and measurement results for the 360-RS, P-RS, and traditional SFM-PC when $\theta = 0°$ (a) $|S_{11}|$ for ON state, (b) $|S_{12}|$ for ON state, (c) $|S_{11}|$ for OFF state, (d) $|S_{12}|$ for OFF state.

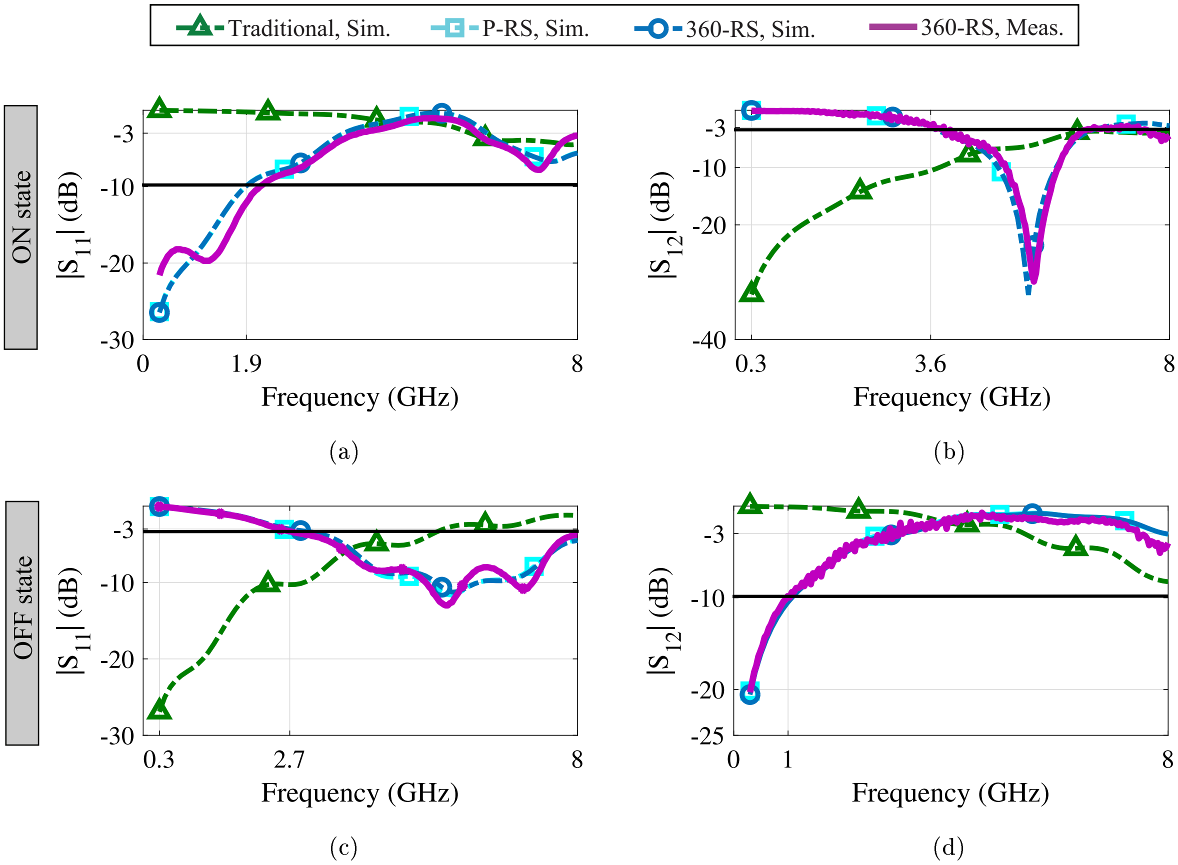

(a) (b) (c) (d)

Figure 4.8. Simulation and measurement results for the 360-RS, P-RS, and traditional SFM-PC when $\theta = 90°$ (a) $|S_{11}|$ for ON state, (b) $|S_{12}|$ for ON state, (c) $|S_{11}|$ for OFF state, (d) $|S_{12}|$ for OFF state.

Furthermore, the host transmission line with embedded 360-RS, made of Rogers TMM3, was rotated around the x-axis and its performance (ON state: -10 dB for $|S_{11}|$ and -3 dB for $|S_{12}|$, OFF state: -3 dB for $|S_{11}|$ and -10 dB for $|S_{12}|$) for different angles from the z-axis is illustrated in Fig. 4.9. For $h = 3.18$ mm and $h'' = 2.09$ mm, the 'non-working' angles ranges from 17°-72° and 197°-252° as shown by the grey area in this figure. As can be realized from this figure, the performance of the switch stays the same for different angles implying the reliability and the efficacy of the proposed design. Additionally, it illustrates that the switch and circuit can be rotated after fabrication.

4.4. Conclusion

Novel 360-degree rotatable and partial rotatable radio frequency (RF) switches based on Static Field Micro-Particle Components (SFM-PCs) were proposed. The performance of these

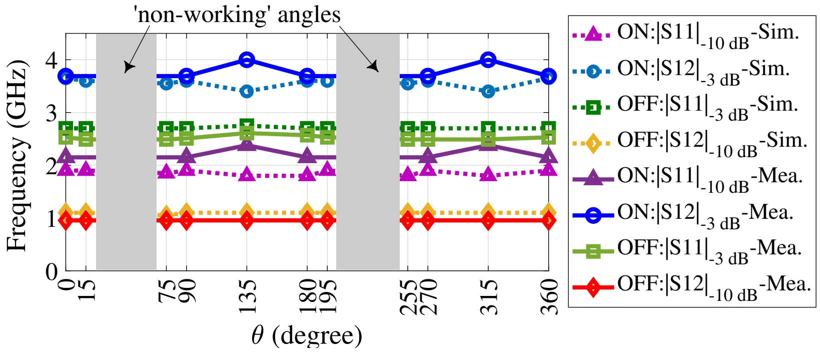

Figure 4.9. Simulated and measured performance of the 360-degree rotatable SFM-PC embedded on the microstrip transmission line (TL).

rotatable SFM-PC switches was evaluated by embedding them on a host microstrip transmission line (TL). HFSS simulation and measurement results reveal that the presented structures perform correctly while undergoing any rotations, making these rotatable particle-based switches a key building block for future RF systems where reducing power consumption is important.

5. OVERALL CONCLUSION

In this research work, the traditional particle-based RF switches were analyzed thoroughly. Based on the developed model, it was shown that the physical characteristic of the switch (dielectric constant, height, width, and length) affect the performance of the ON and OFF states. While reducing the height and length of the switch increases the frequency bandwidth of the ON state, decreasing the dielectric constant, width, and length as well as increasing the height of the switch, provide better isolation during the OFF state. Because meeting the requirement of very high-speed devices by controlling only the physical characteristic of the switch is not possible due to fabrication limitations as well as the tradeoffs, two novel techniques were developed in order to improve the frequency bandwidth of the ON and OFF states. The simulation and measurement results revealed that by employing Asymmetric Copper (AC) and Double Switch (DSw), the frequency bandwidth can reach up to 7.0 GHz several times the previously reported values. Finally, the rotation issue of the traditional particle-based switches, was addressed by proposing a new 360-degree rotatable structure. The performance of the developed rotatable structure was evaluated by embedding it into microstrip transmission line (TL) and both HFSS simulations and measurements in the anechoic chamber proved the effectiveness of the new design.

REFERENCES

[1] J. R. De Luis and F. De Flaviis. Frequency agile switched beam antenna array system. *IEEE Transactions on Antennas and Propagation*, 58(10):3196–3204, Oct 2010.

[2] R. K. Singh, A. Basu, and S. K. Koul. A novel reconfigurable microstrip patch antenna with polarization agility in two switchable frequency bands. *IEEE Transactions on Antennas and Propagation*, pages 5608–5613, 2018.

[3] H. H. Tran, N. Nguyen-Trong, T. K. Nguyen, and A. M. Abbosh. Bandwidth enhancement utilizing bias circuit as parasitic elements in a reconfigurable circularly polarized antenna. *IEEE Antennas and Wireless Propagation Letters*, 17(8):1533–1537, Aug 2018.

[4] M. Shirazi, T. Li, J. Huang, and X. Gong. A reconfigurable dual-polarization slot-ring antenna element with wide bandwidth for array applications. *IEEE Transactions on Antennas and Propagation*, pages 5943–5954, 2018.

[5] I. Kim and Y. Rahmat-Samii. Rf mems switchable slot patch antenna integrated with bias network. *IEEE Transactions on Antennas and Propagation*, 59(12):4811–4815, Dec 2011.

[6] P. D. Grant, M. W. Denhoff, and R. R. Mansour. A comparison between rf mems switches and semiconductor switches. In *2004 International Conference on MEMS, NANO and Smart Systems (ICMENS'04)*, pages 515–521, Aug 2004.

[7] Fan Yang and Y. Rahmat-Samii. A reconfigurable patch antenna using switchable slots for circular polarization diversity. *IEEE Microwave and Wireless Components Letters*, 12(3):96–98, March 2002.

[8] J. T. Bernhard, R. Wang, R. Clark, and P. Mayes. Stacked reconfigurable antenna elements for space-based radar applications. In *IEEE Antennas and Propagation Society International Symposium. 2001 Digest. Held in conjunction with: USNC/URSI National Radio Science Meeting (Cat. No.01CH37229)*, volume 1, pages 158–161 vol.1, July 2001.

[9] Jung-Chih Chiao, Yiton Fu, Iao Mak Chio, M. DeLisio, and Lih-Yuan Lin. Mems reconfigurable vee antenna. In *1999 IEEE MTT-S International Microwave Symposium Digest (Cat. No.99CH36282)*, volume 4, pages 1515–1518 vol.4, June 1999.

[10] E. R. Brown. Rf-mems switches for reconfigurable integrated circuits. *IEEE Transactions on Microwave Theory and Techniques*, 46(11):1868–1880, Nov 1998.

[11] Jung-Chih Chiao, Yiton Fu, D. Choudhury, and Lih-Yuan Lin. Mems millimeterwave components. In *1999 IEEE MTT-S International Microwave Symposium Digest (Cat. No.99CH36282)*, volume 2, pages 463–466 vol.2, June 1999.

[12] Xue-Song Yang, Bing-Zhong Wang, and Yong Zhang. A reconfigurable hilbert curve patch antenna. In *2005 IEEE Antennas and Propagation Society International Symposium*, volume 2B, pages 613–616 vol. 2B, July 2005.

[13] A. C. K. Mak, C. R. Rowell, R. D. Murch, and C. Mak. Reconfigurable multiband antenna designs for wireless communication devices. *IEEE Transactions on Antennas and Propagation*, 55(7):1919–1928, July 2007.

[14] J. M. Parrow and et al. On the bandwidth of a microparticle-based component responsive to magnetostatic fields. *IEEE Transactions on Electromagnetic Compatibility*, 59(4):1053–1059, Aug 2017.

[15] A. Iftikhar, J. Parrow, S. Asif, J. Allen, M. Allen, and B. D. Braaten. Improving the efficiency of a reconfigurable microstrip patch using magneto-static field responsive structures. *Electronics Letters*, 52(14):1194–1196, 2016.

[16] A. Iftikhar and et al. On using magneto-static responsive particles as switching elements to reconfigure microwave filters. In *2016 IEEE International Conference on Electro Information Technology (EIT)*, pages 192–195, May 2016.

[17] A. Iftikhar, J. M. Parrow, S. M. Asif, S. Z. Sajal, B. D. Braaten, J. Allen, M. Allen, and B. Wenner. A printed dipole reconfigured with magneto-static responsive structures that do not require a directly connected biasing circuit. In *2016 IEEE International Symposium on Antennas and Propagation (APSURSI)*, pages 1057–1058, June 2016.

[18] J. M. Parrow, A. Iftikhar, S. M. Asif, B. D. Braaten, J. W. Allen, M. S. Allen, and B. R. Wenner. On controlling the propagation characteristics of microstrip transmission lines using embedded micron-sized particles and static h-fields. In *2017 IEEE International Symposium on Antennas and Propagation USNC/URSI National Radio Science Meeting*, pages 2269–2270, July 2017.

[19] Fan Yang and Y. Rahmat-Samii. A reconfigurable patch antenna using switchable slots for circular polarization diversity. *IEEE Microwave and Wireless Components Letters*, 12(3):96–98, March 2002.

[20] D.M. Pozar. *Microwave Engineering*. Wiley, 2004.

[21] N. Soufizadeh-Balaneji, D. A. Rogers, and B. D. Braaten. An imporved model for static field micro-particle components on a printed tranmission line. In *2019 IEEE International Symposium on Antennas and Propagation (APS/URSI)*, July 2019.

APPENDIX

The reflection coefficients of the traditional SSwSC when the slopped part of the copper foil approximated by 2-segment, 3-segment, and 4-segment were calculated in the appendix. Note that the extracted formulas can be applied for SSwAC with D_i from (3.9).

A 2-segment approximation: The slopped part of the copper foil was approximated using two equally-spaced segments with the lengths $\Delta l_c = \frac{l_c}{2}$ and heights h_{sw} and $\frac{h_{sw}}{2}$ as illustrated in Fig. A.1. Assuming the lossless line, the characteristic impedances in each of the regions are given by

$$\text{Region } 3 : Z_{0,3} = \sqrt{\frac{L_3}{C_3}} = Z_0 \times D_3, \tag{A.1}$$

$$\text{Region } 2 : Z_{0,2} = \sqrt{\frac{L_2}{C_2}} = Z_0 \times D_2, \tag{A.2}$$

and

$$\text{Region } 1 : Z_{0,1} = \sqrt{\frac{L_1}{C_1}} = Z_0 \times D_1. \tag{A.3}$$

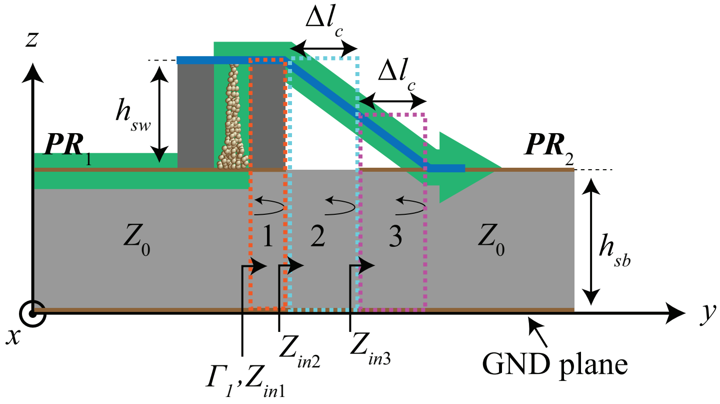

Figure A.1. 2-segment approximation of the copper foil.

Using the characteristic impedances, the input impedances Z_{in1}, Z_{in2}, and Z_{in3} can be calculated as

$$Z_{in3} = Z_3 \frac{Z_0 + jZ_3 \tan(\beta_3 \Delta l_c)}{Z_3 + jZ_0 \tan(\beta_3 \Delta l_c)} = Z_0 \times D_3 \frac{1 + jD_3 \tan(\beta_3 \Delta l_c)}{D_3 + j \tan(\beta_3 \Delta l_c)}, \tag{A.4}$$

$$\begin{aligned} Z_{in2} =& Z_2 \frac{Z_{in3} + jZ_2 \tan(\beta_2 \Delta l_c)}{Z_2 + jZ_{in3} \tan(\beta_2 \Delta L_c)} = \\ & Z_0 \times D_2 \frac{D_3 + j(D_3)^2 \tan(\beta_3 \Delta l_c) + jD_2 D_3 \tan(\beta_2 \Delta l_c) - D_2 \tan(\beta_2 \Delta l_c) \tan(\beta_3 \Delta l_c)}{D_2 D_3 + jD_2 \tan(\beta_3 \Delta l_c) + jD_3 \tan(\beta_2 \Delta l_c) - (D_3)^2 \tan(\beta_2 \Delta l_c) \tan(\beta_3 \Delta l_c)}, \end{aligned} \tag{A.5}$$

and

$$Z_{in1} = Z_0 \times D_1 \frac{Z_{in2} + jZ_0 D_1 tan(\beta_1 l_1)}{Z_0 D_1 + jZ_{in2} tan(\beta_1 l_1)}. \tag{A.6}$$

The voltage reflection coefficient can be obtained using the input imepadnces which is given by

$$\Gamma_1 = \frac{Z_{in1} - Z_0}{Z_{in1} + Z_0} = \frac{\Gamma_1|_{numer.}}{\Gamma_1|_{denom.}}, \tag{A.7}$$

where its numerator and denominator are from

$$\begin{aligned} \Gamma_1|_{numer.} =& jD_1 D_2 \tan(\beta_3 \Delta l_c) \times [(D_3)^2 - 1] + jD_1 D_3 \tan(\beta_2 \Delta l_c)[(D_2)^2 - 1] \\ & + jD_2 D_3 \tan(\beta_1 l_1)[(D_1)^2 - 1] + D_3 \tan(\beta_1 l_1) \tan(\beta_2 \Delta l_c)[(D_2)^2 - (D_1)^2] \\ & + D_2 \tan(\beta_1 l_1) \tan(\beta_3 \Delta l_c)[(D_3)^2 - (D_1)^2] + D_1 \tan(\beta_2 \Delta l_c) \tan(\beta_3 \Delta l_c)[(D_3)^2 - (D_2)^2] \\ & + j \tan(\beta_1 l_1) \tan(\beta_2 \Delta l_c) \tan(\beta_3 \Delta l_c)[(D_2)^2 - (D_1)^2 (D_3)^2] \end{aligned} \tag{A.8}$$

and

$$\begin{aligned} \Gamma_1|_{denom.} =& 2D_1 D_2 D_3 + jD_1 D_2 \tan(\beta_3 \Delta l_c)[(D_3)^2 + 1] + jD_1 D_3 \tan(\beta_2 \Delta l_c)[(D_2)^2 + 1] \\ & + jD_2 D_3 \tan(\beta_1 l_1)[(D_1)^2 + 1] - D_1 \tan(\beta_2 \Delta l_c) \tan(\beta_3 \Delta l_c)[(D_2)^2 + (D_3)^2] \\ & - D_2 \tan(\beta_1 l_1) \tan(\beta_3 \Delta l_c)[(D_1)^2 + (D_3)^2] - D_3 \tan(\beta_2 \Delta l_c) \tan(\beta_1 l_1)[(D_1)^2 + (D_2)^2] \\ & - j \tan(\beta_1 l_1) \tan(\beta_2 \Delta l_c) \tan(\beta_3 \Delta l_c)[(D_2)^2 + (D_1)^2 (D_3)^2]. \end{aligned} \tag{A.9}$$

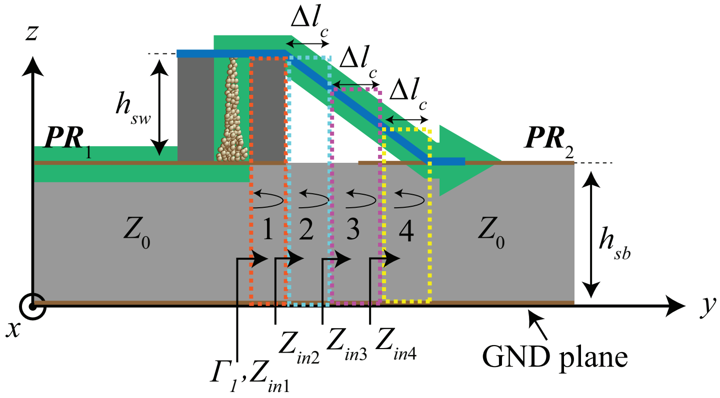

Figure A.2. 3-segment approximation of the copper foil.

A 3-segment approximation: For a 3-segment approximation, the second region was approximated using three segments with the lengths $\Delta l_c = \frac{l_c}{3}$ and heights h_{sw}, $\frac{2h_{sw}}{3}$, and $\frac{h_{sw}}{3}$ shown in Fig. A.2. The characteristic impedances of the created regions can be obtained by

$$\text{Region } 4 : Z_{0,4} = Z_0 \times D_4, \tag{A.10}$$

$$\text{Region } 3 : Z_{0,3} = Z_0 \times D_3, \tag{A.11}$$

$$\text{Region } 2 : Z_{0,2} = Z_0 \times D_2, \tag{A.12}$$

and

$$\text{Region } 1 : Z_{0,1} = Z_0 \times D_1. \tag{A.13}$$

Based on the equations above, the input impedances can be calculated from the below equations.

$$Z_{in4} = Z_4 \frac{Z_0 + jZ_4 \tan(\beta_4 \Delta l_c)}{Z_4 + jZ_0 \tan(\beta_4 \Delta l_c)} = Z_0 \times D_4 \times \frac{1 + jD_4 \tan(\beta_4 \Delta l_c)}{D_4 + j\tan(\beta_4 \Delta l_c)}, \tag{A.14}$$

$$\begin{aligned}Z_{in3} =& Z_3\frac{Z_{in4} + jZ_3\tan(\beta_3\Delta l_c)}{Z_3 = jZ_{in4}\tan(\beta_3\Delta l_c)} = \\ & Z_0 \times D_3 \times \frac{D_4 + j(D_4)^2\tan(\beta_4\Delta l_c) + jD_3D_4\tan(\beta_3\Delta l_c) - D_3\tan(\beta_3\Delta l_c)\tan(\beta_4\Delta l_c)}{D_3D_4 + jD_3\tan(\beta_4\Delta l_c) + jD_4\tan(\beta_3\Delta l_c) - (D_4)^2\tan(\beta_4\Delta l_c)\tan(\beta_3\Delta l_c)},\end{aligned} \tag{A.15}$$

$$Z_{in2} = Z_2\frac{Z_{in3} + jZ_2\tan(\beta_2\Delta l_c)}{Z_2 + jZ_{in3}\tan(\beta_2\Delta l_c)} = Z_0D_2\frac{Z_{in2}|_{numer.}}{Z_{in2}|_{denom.}}, \tag{A.16}$$

where its numerator and denominator are given by (A. 17) and (A.18).

$$\begin{aligned}Z_{in2}|_{numer.} =& D_3D_4 + jD_3(D_4)^2\tan(\beta_4\Delta l_c) + j(D_3)^2D_4\tan(\beta_4\Delta l_c) - (D_3)^2\tan(\beta_3\Delta l_c) \\ & + jD_2D_3D_4\tan(\beta_2\Delta l_c) - D_2D_3\tan(\beta_2\Delta l_c)\tan(\beta_4\Delta l_c) - D_2D_4\tan(\beta_2\Delta l_c)\tan(\beta_3\Delta l_c) \\ & - jD_2(D_4)^2\tan(\beta_2\Delta l_c)\tan(\beta_3\Delta l_c)\tan(\beta_4\Delta l_c)\end{aligned} \tag{A.17}$$

$$\begin{aligned}Z_{in2}|_{denom.} =& D_2D_3D_4 + jD_2D_3\tan(\beta_4\Delta l_c) + jD_2D_4\tan(\beta_3\Delta l_c) - D_2(D_4)^2\tan(\beta_4\Delta l_c) \\ & + jD_3D_4\tan(\beta_2\Delta l_c) - D_3(D_4)^2\tan(\beta_2\Delta l_c)\tan(\beta_4\Delta l_c) - (D_3)^2D_4\tan(\beta_2\Delta l_c) \\ & - j(D_3)^2\tan(\beta_2\Delta l_c)\tan(\beta_3\Delta l_c)\tan(\beta_4\Delta l_c)\end{aligned} \tag{A.18}$$

$$Z_{in1} = Z_1\frac{Z_{in2} + jZ_1tan(\beta_1l_1)}{Z_1 + jZ_{in2}tan(\beta_1l_1)} = Z_0D_1\frac{Z_{in1}|_{numer.}}{Z_{in2}|_{denom.}}. \tag{A.19}$$

Using the input impedances Z_{in1}, Z_{in2}, and Z_{in3}, the reflection coefficient in Fig. A.2 is given by

$$\Gamma_1 = \frac{Z_{in1} - Z_0}{Z_{in1} + Z_0} = \frac{\Gamma_1|_{numer.}}{\Gamma_1|_{denom.}}, \tag{A.20}$$

where its numerator and denominator are from

$$\begin{aligned}\Gamma_1|_{numer.} =& jD_1D_2D_3\tan(\beta_4\Delta l_c)[(D_4)^2 - 1] + jD_1D_2D_4\tan(\beta_3\Delta l_c)[(D_3)^2 - 1] \\ & + jD_1D_3D_4\tan(\beta_2\Delta l_c)[(D_2)^2 - 1] + jD_2D_3D_4\tan(\beta_1l_1)[(D_1)^2 - 1] \\ & + D_1D_2\tan(\beta_3\Delta l_c)\tan(\beta_4\Delta l_c)[(D_4)^2 - (D_3)^2]\end{aligned}$$

$$
\begin{aligned}
&+ D_1D_3\tan(\beta_2\Delta l_c)\tan(\beta_4\Delta l_c)[(D_4)^2-(D_2)^2]\\
&+ D_1D_4\tan(\beta_2\Delta l_c)\tan(\beta_3\Delta l_c)[(D_3)^2-(D_2)^2]\\
&+ D_2D_3\tan(\beta_1 l_1)\tan(\beta_4\Delta l_c)[(D_4)^2-(D_1)^2]\\
&+ D_2D_4\tan(\beta_1 l_1)\tan(\beta_3\Delta l_c)[(D_3)^2-(D_1)^2]\\
&+ D_3D_4\tan(\beta_1 l_1)\tan(\beta_2\Delta l_c)[(D_2)^2-(D_1)^2]\\
&+ jD_1\tan(\beta_2\Delta l_c)\tan(\beta_3\Delta l_c)\tan(\beta_4\Delta l_c)[(D_3)^2-(D_2)^2(D_4)^2]\\
&+ jD_2\tan(\beta_1 l_1)\tan(\beta_3\Delta l_c)\tan(\beta_4\Delta l_c)[(D_3)^2-(D_1)^2(D_4)^2]\\
&+ jD_3\tan(\beta_1 l_1)\tan(\beta_2\Delta l_c)\tan(\beta_4\Delta l_c)[(D_2)^2-(D_1)^2(D_4)^2]\\
&+ jD_4\tan(\beta_1 l_1)\tan(\beta_2\Delta l_c)\tan(\beta_3\Delta l_c)[(D_2)^2-(D_1)^2(D_3)^2]\\
&+ \tan(\beta_1 l_1)\tan(\beta_2\Delta l_c)\tan(\beta_3\Delta l_c)\tan(\beta_4\Delta l_c)[(D_1)^2(D_3)^2-(D_2)^2(D_4)^2] \qquad \text{(A.21)}
\end{aligned}
$$

$$
\begin{aligned}
\Gamma_1|_{denom.} =& 2D_1D_2D_3D_4 + jD_1D_2D_3\tan(\beta_4\Delta l_c)[(D_4)^2+1] + jD_1D_2D_4\tan(\beta_3\Delta l_c)[(D_3)^2+1]\\
&+ jD_1D_3D_4\tan(\beta_2\Delta l_c)[(D_2)^2+1] + jD_2D_3D_4\tan(\beta_1 l_1)[(D_1)^2+1]\\
&- D_1D_2\tan(\beta_3\Delta l_c)\tan(\beta_4\Delta l_c)[(D_4)^2+(D_3)^2]\\
&- D_1D_3\tan(\beta_2\Delta l_c)\tan(\beta_4\Delta l_c)[(D_4)^2+(D_2)^2]\\
&- D_1D_4\tan(\beta_2\Delta l_c)\tan(\beta_3\Delta l_c)[(D_3)^2+(D_2)^2]\\
&- D_2D_3\tan(\beta_1 l_1)\tan(\beta_4\Delta l_c)[(D_4)^2+(D_1)^2]\\
&- D_2D_4\tan(\beta_1 l_1)\tan(\beta_3\Delta l_c)[(D_3)^2+(D_1)^2]\\
&- D_3D_4\tan(\beta_1 l_1)\tan(\beta_2\Delta l_c)[(D_2)^2+(D_1)^2]\\
&- jD_1\tan(\beta_2\Delta l_c)\tan(\beta_3\Delta l_c)\tan(\beta_4\Delta l_c)[(D_3)^2+(D_2)^2(D_4)^2]\\
&- jD_2\tan(\beta_1 l_1)\tan(\beta_3\Delta l_c)\tan(\beta_4\Delta l_c)[(D_3)^2+(D_1)^2(D_4)^2]\\
&- jD_3\tan(\beta_1 l_1)\tan(\beta_2\Delta l_c)\tan(\beta_4\Delta l_c)[(D_2)^2+(D_1)^2(D_4)^2]\\
&- jD_4\tan(\beta_1 l_1)\tan(\beta_2\Delta l_c)\tan(\beta_3\Delta l_c)[(D_2)^2+(D_1)^2(D_3)^2]\\
&+ \tan(\beta_1 l_1)\tan(\beta_2\Delta l_c)\tan(\beta_3\Delta l_c)\tan(\beta_4\Delta l_c)[(D_1)^2(D_3)^2+(D_2)^2(D_4)^2] \qquad \text{(A.22)}
\end{aligned}
$$

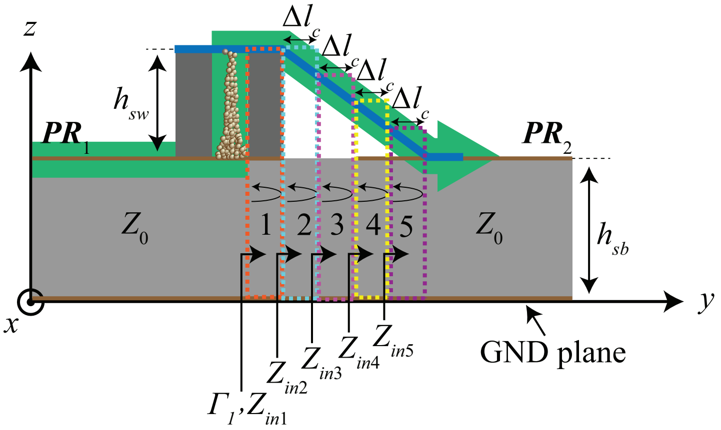

Figure A.3. 4-segment approximation of the copper foil.

A 4-segment approximation: The second part of the copper foil was approximated using four segments with the lengths $\Delta l_c = \frac{l_c}{4}$ and heights h_{sw}, $\frac{3h_{sw}}{4}$, $\frac{h_{sw}}{2}$, and $\frac{h_{sw}}{4}$. The characteristic impedances in each of these regions are given by

$$\text{Region } 5 : Z_{0,5} = \sqrt{\frac{L_5}{C_5}} = Z_0 \times D_5, \tag{A.23}$$

$$\text{Region } 4 : Z_{0,4} = \sqrt{\frac{L_4}{C_4}} = Z_0 \times D_4, \tag{A.24}$$

$$\text{Region } 3 : Z_{0,3} = \sqrt{\frac{L_3}{C_3}} = Z_0 \times D_3, \tag{A.25}$$

$$\text{Region } 2 : Z_{0,2} = \sqrt{\frac{L_2}{C_2}} = Z_0 \times D_2, \tag{A.26}$$

and

$$\text{Region } 1 : Z_{0,1} = \sqrt{\frac{L_1}{C_1}} = Z_0 \times D_1. \tag{A.27}$$

Based on calculated characteristic impedances, the input impedances can be obtained from the following equations.

$$Z_{in5} = Z_5 \frac{Z_0 + jZ_5 \tan(\beta_5 \Delta l_c)}{Z_5 + jZ_0 \tan(\beta_5 \Delta l_c)} = Z_0 D_5 \frac{1 + jD_5 \tan(\beta_5 \Delta l_c)}{D_5 + j \tan(\beta_5 \Delta l_c)} \tag{A.28}$$

$$\begin{aligned}Z_{in4} =& Z_4\frac{Z_{in5}+jZ_4\tan(\beta_4\Delta l_c)}{Z_4+jZ_{in5}\tan(\beta_4\Delta l_c)}\\ =& Z_0D_4\frac{D_5+j(D_5)^2\tan(\beta_5\Delta l_c)+jD_4D_5\tan(\beta_4\Delta l_c)-D_4\tan(\beta_4\Delta l_c)\tan(\beta_5\Delta l_c)}{D_4D_5+jD_4\tan(\beta_5\Delta l_c)+jD_5\tan(\beta_4\Delta l_c)-(D_5)^2\tan(\beta_4\Delta l_c)\tan(\beta_5\Delta l_c)}\end{aligned} \tag{A.29}$$

$$Z_{in3} = Z_3\frac{Z_{in4}+jZ_3\tan(\beta_3\Delta l_c)}{Z_3+jZ_{in4}\tan(\beta_3\Delta l_c)} = Z_0D_3\frac{Z_{in3}|_{numer.}}{Z_{in3}|_{denom.}}, \tag{A.30}$$

where its numerator and denominator are given by (A.31) and (A.32).

$$\begin{aligned}Z_{in3}|_{numer.} =& D_4D_5+jD_4(D_5)^2\tan(\beta_5\Delta l_c)+j(D_4)^2D_5\tan(\beta_4\Delta l_c)-(D_4)^2\tan(\beta_4\Delta l_c)\tan(\beta_5\Delta l_c)\\ &+jD_3D_4D_5\tan(\beta_3\Delta l_c)-D_3D_4\tan(\beta_3\Delta l_c)\tan(\beta_5\Delta l_c)-D_3D_5\tan(\beta_3\Delta l_c)\tan(\beta_4\Delta l_c)\\ &-jD_3(D_5)^2\tan(\beta_3\Delta l_c)\tan(\beta_4\Delta l_c)\tan(\beta_5\Delta l_c)\end{aligned} \tag{A.31}$$

$$\begin{aligned}Z_{in3}|_{denom.} =& D_3D_4D_5+jD_3D_4\tan(\beta_5\Delta l_c)+jD_3D_5\tan(\beta_4\Delta l_c)-D_3(D_5)^2\tan(\beta_4\Delta l_c)\tan(\beta_5\Delta l_c)\\ &+jD_4D_5\tan(\beta_3\Delta l_c)-D_4(D_5)^2\tan(\beta_3\Delta l_c)\tan(\beta_5\Delta l_c)\\ &-(D_4)^2D_5\tan(\beta_3\Delta l_c)\tan(\beta_4\Delta l_c)-j(D_4)^2\tan(\beta_3\Delta l_c)\tan(\beta_4\Delta l_c)\tan(\beta_5\Delta l_c)\end{aligned} \tag{A.32}$$

$$Z_{in2} = Z_2\frac{Z_{in3}+jZ_2\tan(\beta_2\Delta l_c)}{Z_2+jZ_{in3}\tan(\beta_2\Delta l_c)} = Z_0D_2\frac{Z_{in2}|_{numer.}}{Z_{in2}|_{denom.}} \tag{A.33}$$

$$Z_{in1} = Z_1\frac{Z_{in2}+jZ_1\tan(\beta_1 l_1)}{Z_1+jZ_{in2}\tan(\beta_1 l_1)} = Z_0D_1\frac{Z_{in1}|_{numer.}}{Z_{in1}|_{denom.}} \tag{A.34}$$

Using the input impedances, the voltage reflection coefficient can be formulated as (A.35), where its numerator and denominator are from (A.36) and (A.37).

$$\Gamma_1 = \frac{Z_{in1}-Z_0}{Z_{in1}+Z_0} = \frac{\Gamma_1|_{numer.}}{\Gamma_1|_{denom.}} \tag{A.35}$$

$$\begin{aligned}\Gamma_1|_{numer.} =& jD_1D_3D_4D_5\tan(\beta_2\Delta l_c)[(D_2)^2-1]+jD_2D_3D_4D_5\tan(\beta_1 l_1)[(D_1)^2-1]\\ &+jD_1D_2D_3D_4\tan(\beta_5\Delta l_c)[(D_5)^2-1]+jD_1D_2D_3D_5\tan(\beta_4\Delta l_c)[(D_4)^2-1]\end{aligned}$$

$$+jD_1D_2D_4D_5\tan(\beta_3\Delta l_c)[(D_3)^2-1]+D_1D_3D_4\tan(\beta_2\Delta l_c)\tan(\beta_5\Delta l_c)[(D_5)^2-(D_2)^2]$$

$$+D_1D_3D_5\tan(\beta_2\Delta l_c)\tan(\beta_4\Delta l_c)[(D_4)^2-(D_2)^2]$$

$$+D_2D_3D_4\tan(\beta_1 l_1)\tan(\beta_5\Delta l_c)[(D_5)^2-(D_1)^2]$$

$$+D_2D_3D_5\tan(\beta_1 l_1)\tan(\beta_4\Delta l_c)[(D_4)^2-(D_1)^2]$$

$$+D_2D_4D_5\tan(\beta_1 l_1)\tan(\beta_3\Delta l_c)[(D_3)^2-(D_1)^2]$$

$$+D_1D_2D_3\tan(\beta_4\Delta l_c)tan(\beta_5\Delta l_c)[(D_5)^2-(D_4)^2]$$

$$+D_1D_2D_4\tan(\beta_3\Delta l_c)\tan(\beta_5\Delta l_c)[(D_5)^2-(D_3)^2]$$

$$+D_1D_2D_5\tan(\beta_3\Delta l_c)\tan(\beta_4\Delta l_c)[(D_4)^2-(D_3)^2]$$

$$+D_3D_4D_5\tan(\beta_1 l_1)\tan(\beta_2\delta l_c)[(D_2)^2-(D_1)^2]$$

$$+D_1D_4D_5\tan(\beta_2\Delta l_c)\tan(\beta_3\Delta l_c)[(D_3)^2-(D_2)^2]$$

$$+jD_1D_3\tan(\beta_2\Delta l_c)\tan(\beta_4\Delta l_c)\tan(\beta_5\Delta l_c)[(D_4)^2-(D_2)^2(D_5)^2]$$

$$+jD_1D_4\tan(\beta_2\Delta l_c)\tan(\beta_3\Delta l_c)\tan(\beta_5\Delta l_c)[(D_3)^2-(D_2)^2(D_5)^2]$$

$$+jD_1D_5\tan(\beta_2\Delta l_c)\tan(\beta_3\Delta l_c)\tan(\beta_4\Delta l_c)[(D_3)^2-(D_2)^2(D_4)^2]$$

$$+jD_2D_3\tan(\beta_1 l_1)\tan(\beta_4\Delta l_c)\tan(\beta_5\Delta l_c)[(D_4)^2-(D_1)^2(D_5)^2]$$

$$+jD_2D_4\tan(\beta_1 l_1)\tan(\beta_3\Delta l_c)\tan(\beta_5\Delta l_c)[(D_3)^2-(D_1)^2(D_5)^2]$$

$$+jD_2D_5\tan(\beta_1 l_1)\tan(\beta_3\Delta l_c)\tan(\beta_4\Delta l_c)[(D_3)^2-(D_1)^2(D_4)^2]$$

$$+jD_1D_2\tan(\beta_3\Delta l_c)\tan(\beta_4\Delta l_c)\tan(\beta_5\Delta l_c)[(D_4)^2-(D_3)^2(D_5)^2]$$

$$+jD_3D_5\tan(\beta_1 l_1)\tan(\beta_2\Delta l_c)\tan(\beta_4\Delta l_c)[(D_2)^2-(D_1)^2(D_4)^2]$$

$$+jD_3D_4\tan(\beta_1 l_1)\tan(\beta_2\Delta l_c)\tan(\beta_5\Delta l_c)[(D_2)62-(D_1)^2(D_5)^2]$$

$$+jD_4D_5\tan(\beta_1 l_1)\tan(\beta_2\Delta l_c)\tan(\beta_3\Delta l_c)[(D_2)^2-(D_1)^2(D_3)^2]$$

$$+D_1\tan(\beta_2\Delta l_c)\tan(\beta_3\Delta l_c)\tan(\beta_4\Delta l_c)\tan(\beta_5\Delta l_c)[(D_2)^2(D_4)^2-(D_3)^2(D_5)^2]$$

$$+D_2\tan(\beta_1 l_1)\tan(\beta_3\Delta l_c)\tan(\beta_4\Delta l_c)\tan(\beta_5\Delta l_c)[(D_1)^2(D_4)^2-(D_3)^2(D_5)^2]$$

$$+D_3\tan(\beta_1 l_1)\tan(\beta_2\Delta l_c)\tan(\beta_4\Delta l_c)\tan(\beta_5\Delta l_c)[(D_1)^2(D_4)^2-(D_2)^2(D_5)^2]$$

$$+D_4\tan(\beta_1 l_1)tan(\beta_2\Delta l_c)\tan(\beta_3\Delta l_c)\tan(\beta_5\Delta l_c)[(D_1)^2(D_3)^2-(D_2)^2(D_5)^2]$$

$$+D_5\tan(\beta_1 l_1)tan(\beta_2\Delta l_c)\tan(\beta_3\Delta l_c)\tan(\beta_4\Delta l_c)[(D_1)^2(D_3)^2-(D_2)^2(D_4)^2]$$

$$+j\tan(\beta_1 l_1)\tan(\beta_2\Delta l_c)\tan(\beta_3\Delta l_c)\tan(\beta_4\Delta l_c)\tan(\beta_5\Delta l_c)[(D_1)^2(D_3)^2(D_5)^2$$

$$-(D_2)^2(D_4)^2] \tag{A.36}$$

$$\begin{aligned}
\Gamma_1|_{denom.} =& 2D_1D_2D_3D_4D_5 + jD_1D_3D_4D_5\tan(\beta_2\Delta l_c)[(D_2)^2+1] \\
&+jD_2D_3D_4D_5\tan(\beta_1 l_1)[(D_1)^2+1] \\
&+jD_1D_2D_3D_4\tan(\beta_5\Delta l_c)[(D_5)^2+1] + jD_1D_2D_3D_5\tan(\beta_4\Delta l_c)[(D_4)^2+1] \\
&+jD_1D_2D_4D_5\tan(\beta_3\Delta l_c)[(D_3)^2+1] \\
&-D_1D_3D_4\tan(\beta_2\Delta l_c)\tan(\beta_5\Delta l_c)[(D_5)^2+(D_2)^2] \\
&-D_1D_3D_5\tan(\beta_2\Delta l_c)\tan(\beta_4\Delta l_c)[(D_4)^2+(D_2)^2] \\
&-D_2D_3D_4\tan(\beta_1 l_1)\tan(\beta_5\Delta l_c)[(D_5)^2+(D_1)^2] \\
&-D_2D_3D_5\tan(\beta_1 l_1)\tan(\beta_4\Delta l_c)[(D_4)^2+(D_1)^2] \\
&-D_2D_4D_5\tan(\beta_1 l_1)tan(\beta_3\Delta l_c)[(D_3)^2+(D_1)^2] \\
&-D_1D_2D_3\tan(\beta_4\Delta l_c)\tan(\beta_5\Delta l_c)[(D_5)^2+(D_4)^2] \\
&-D_1D_2D_4\tan(\beta_3\Delta l_c)\tan(\beta_5\Delta l_c)[(D_5)^2+(D_3)^2] \\
&-D_1D_2D_5\tan(\beta_3\Delta l_c)\tan(\beta_4\Delta l_c)[(D_4)^2+(D_3)^2] \\
&-D_3D_4D_5\tan(\beta_1 l_1)\tan(\beta_2\Delta l_c)[(D_2)^2+(D_1)^2] \\
&-D_1D_4D_5\tan(\beta_2\Delta l_c)\tan(\beta_3\Delta l_c)[(D_3)^2+(D_2)^2] \\
&-jD_1D_3\tan(\beta_2\Delta l_c)\tan(\beta_4\Delta l_c)\tan(\beta_5\Delta l_c)[(D_4)^2+(D_2)^2(D_5)^2] \\
&-jD_1D_4\tan(\beta_2\Delta l_c)\tan(\beta_3\Delta l_c)\tan(\beta_5\Delta l_c)[(D_3)^2+(D_2)^2(D_5)^2] \\
&-jD_1D_5\tan(\beta_2\Delta l_c)\tan(\beta_3\Delta l_c)\tan(\beta_4\Delta l_c)[(D_3)^2+(D_2)^2(D_4)^2] \\
&-jD_2D_3\tan(\beta_1 l_1)\tan(\beta_4\Delta l_c)\tan(\beta_5\Delta l_c)[(D_4)^2+(D_1)^2(D_5)^2] \\
&-jD_2D_4\tan(\beta_1 l_1)\tan(\beta_3\Delta l_c)\tan(\beta_5\Delta l_c)[(D_3)^2+(D_1)^2(D_5)^2] \\
&-jD_2D_5\tan(\beta_1 l_1)\tan(\beta_3\Delta l_c)\tan(\beta_4\Delta l_c)[(D_3)^2+(D_1)^2(D_4)^2] \\
&-jD_1D_2\tan(\beta_3\Delta l_c)\tan(\beta_4\Delta l_c)\tan(\beta_5\Delta l_c)[(D_4)^2+(D_3)^2(D_5)^2] \\
&-jD_3D_5\tan(\beta_1 l_1)\tan(\beta_2\Delta l_c)\tan(\beta_4\Delta l_c)[(D_2)^2+(D_1)^2(D_4)^2] \\
&-jD_3D_4\tan(\beta_1 l_1)\tan(\beta_2\Delta l_c)\tan(\beta_5\Delta l_c)[(D_2)^2+(D_1)^2(D_5)^2]
\end{aligned}$$

$$
\begin{aligned}
&-jD_4D_5\tan(\beta_1 l_1)\tan(\beta_2\Delta l_c)\tan(\beta_3\Delta l_c)[(D_2)^2+(D_1)^2(D_3)^2]\\
&+D_1\tan(\beta_2\Delta l_c)\tan(\beta_3\Delta l_c)\tan(\beta_4\Delta l_c)\tan(\beta_5\Delta l_c)[(D_2)^2(D_4)^2+(D_3)^2(D_5)^2]\\
&+D_2\tan(\beta_1 l_1)\tan(\beta_3\Delta l_c)\tan(\beta_4\Delta l_c)\tan(\beta_5\Delta l_c)[(D_1)^2(D_4)^2+(D_3)^2(D_5)^2]\\
&+D_3\tan(\beta_1 l_1)\tan(\beta_2\Delta l_c)\tan(\beta_4\Delta l_c)\tan(\beta_5\Delta l_c)[(D_1)^2(D_4)^2+(D_2)^2(D_5)^2]\\
&+D_4\tan(\beta_1 l_1)\tan(\beta_2\Delta l_c)\tan(\beta_3\Delta l_c)\tan(\beta_5\Delta l_c)[(D_1)^2(D_3)^2+(D_2)^2(D_5)^2]\\
&+D_5\tan(\beta_1 l_1)\tan(\beta_2\Delta l_c)\tan(\beta_3\Delta l_c)\tan(\beta_4\Delta l_c)[(D_1)^2(D_3)^2+(D_2)^2(D_4)^2]\\
&+j\tan(\beta_1 l_1)\tan(\beta_2\Delta l_c)\tan(\beta_3\Delta l_c)\tan(\beta_4\Delta l_c)\tan(\beta_5\Delta l_c)[(D_1)^2(D_3)^2(D_5)^2\\
&\qquad\qquad\qquad\qquad\qquad\qquad\qquad\qquad\qquad\qquad+(D_2)^2(D_4)^2] \qquad \text{(A.37)}
\end{aligned}
$$